

THE CONTRIBUTION OF HOST GALAXIES TO THE INFRARED ENERGY OUTPUT OF $z \gtrsim 5.0$ QUASARSJIANWEI LYU (吕建伟)^{1,†}, G. H. RIEKE¹, STACEY ALBERTS¹*Accepted by ApJ September 12, 2021*

ABSTRACT

The infrared spectral energy distributions (SEDs) of $z \gtrsim 5$ quasars can be reproduced by combining a low-metallicity galaxy template with a standard AGN template. The host galaxy is represented by Haro 11, a compact, moderately low metallicity, star-bursting galaxy that shares typical features of high- z galaxies. For the vast majority of $z \gtrsim 5$ quasars, the AGN contribution is well modeled by a standard empirical template with the contamination of star formation in the infrared subtracted. Together, these two templates can separate the contributions from the host galaxy and the AGN even in the case of limited data points, given that this model has only two free parameters. Using this method, we re-analyze 69 $z \gtrsim 5$ quasars with extensive *Herschel* observations, and derive their AGN luminosities L_{AGN} in a range $\sim (0.78 - 27.4) \times 10^{13} L_{\odot}$, the infrared luminosities from star formation $L_{\text{SF,IR}} \sim (< 1.5 - 25.7) \times 10^{12} L_{\odot}$, and the corresponding star formation rates $\text{SFR} \sim (< 290 - 2650) M_{\odot}/\text{yr}$. The average infrared luminosity from star formation and the average total AGN luminosity of the $z \gtrsim 5$ quasar sample follows the correlation defined by quasars at $z < 2.6$. We assume these quasar host galaxies maintain a constant average SFR ($\sim 620 M_{\odot}/\text{yr}$) during their mass assembly and estimate the stellar mass that could form till $z \sim 5 - 6$ to be $\langle M_{*} \rangle \sim (3 - 5) \times 10^{11} M_{\odot}$. Combining with the black hole (BH) mass measurements, this stellar mass is adequate to establish a BH-galaxy mass ratio M_{BH}/M_{*} at 0.1-1%, consistent with the local relation.

Subject headings: galaxies: active – infrared: galaxies – quasars: general – galaxies: dwarf

1. INTRODUCTION

Over 150 quasars with black hole masses of the order of $10^8 - 10^9 M_{\odot}$ have been discovered beyond $z \sim 5$, less than a billion years after the Big Bang (e.g., Fan et al. 2006; Jiang et al. 2008; Mortlock et al. 2009; Willott et al. 2010a; Morganson et al. 2012; McGreer et al. 2013; Bañados et al. 2014). In the local Universe, the masses of supermassive black holes (SMBHs) are correlated with the properties of their host galaxies, suggesting galaxies and SMBHs possibly co-evolve (Kormendy & Ho 2013, and references therein). Since star formation (SF) enables the buildup of galaxies and active galactic nuclei (AGN) trace the growth of SMBHs, the so-called SF-AGN relation has come under intense scrutiny for decades (Heckman & Best 2014, and references therein). With the use of ground- and space-based facilities, similar research can be extended to $z > 5$, allowing the preliminary examination of both the stellar and SMBH growth at very early stages in galaxy evolution (e.g., Walter et al. 2004, 2009; Maiolino et al. 2005; Riechers et al. 2006; Jahnke et al. 2009; Wang et al. 2010b, 2013; Willott et al. 2013, 2015).

However, observing the AGN host galaxy in a quasar is challenging, since the bright continuum emission from the active nucleus overpowers the light from the galaxy from the UV through the near-infrared (near-IR or NIR). At $z > 5$, the situation is even more extreme: the AGN tend to be the most luminous because of the evolution of the quasar luminosity function and selection effects (e.g., Fan et al. 2004; Jiang et al. 2008; Willott et al. 2010b; McGreer et al. 2013); the host galaxies are found to be

compact and small (e.g., Jiang et al. 2013; Wang et al. 2013); and the presence of copious amounts of dust (e.g., Wang et al. 2008b; Leipski et al. 2014) may also obscure the galaxy light. To study these very distant AGN host galaxies, attention has turned to the emission in longer wavelengths (e.g., Wang et al. 2010b, 2011b, 2013; Leipski et al. 2013, 2014), where the AGN is less dominant.

A promising tool to probe the stellar activity in a quasar is analyzing its infrared (IR) spectral energy distribution (SED). For galaxies, most of the radiation from the recently formed stars is absorbed and re-emitted at IR wavelengths. However, in quasars, the central AGN may also heat the dust (e.g., Haas et al. 2003; Netzer et al. 2007). Since spatially resolving the IR emission at high-redshift is impossible with current facilities, we have to rely on SED models to distinguish star formation and nuclear activity (e.g., Marshall et al. 2007; Mullaney et al. 2011; Mor & Netzer 2012; Magdis et al. 2013; Netzer et al. 2014; Xu et al. 2015b,a).

The UV-to-NIR SEDs of AGN seem to have little evolution with redshift and Eddington-ratio (e.g., Hao et al. 2014; Wang et al. 2008b). However, at $z > 5$, the far-IR SEDs of quasars seem to include a warm (40-60 K) dust component (e.g., Beelen et al. 2006; Wang et al. 2008a; Leipski et al. 2014), which is not commonly found in the local quasars. It is intriguing to check if such behavior is due to the evolution of the AGN host galaxies, since the IR SEDs of galaxies do change at high- z (see Lutz 2014 for a review). Compared with local nuclear-concentrated ULIRGs, intermediate redshift ($z \sim 2-3$) dusty star-forming galaxies (DSFGs) are more extended, resulting in cooler SEDs than those locally with similar IR luminosities (Rujopakarn et al. 2011). Meanwhile, galaxies at higher redshifts have more gas

¹ Steward Observatory, University of Arizona, 933 North Cherry Avenue, Tucson, AZ 85721, USA

[†] jianwei@email.arizona.edu

(e.g., Carilli & Walter 2013) to supply the star formation, boosting their IR luminosities (e.g., Daddi et al. 2005, 2007; Rodighiero et al. 2011; Magnelli et al. 2014; Schreiber et al. 2015). Moreover, both observations and theories suggest galaxies in the early Universe are generally metal poor (e.g., Madau & Dickinson 2014, and references therein), which could also have detectable effects on their SEDs, such as weak aromatic features, featureless mid-IR (MIR) continuum, and higher dust temperatures (e.g., Galliano et al. 2005; Rémy-Ruyer et al. 2013). At extremely high redshift (e.g., $z > 4$), direct constraints on metallicity in galaxies are rare; however, indirect evidence supporting low-metallicity comes from the failed detection of the dust continuum for nearly all $z > 6$ galaxies (e.g., Ouchi et al. 2013; Maiolino et al. 2015, but see Watson et al. 2015). It is likely that galaxies, in general, including those quasar host galaxies, are of relatively low-metallicity when the Universe age is within ~ 1 Gyr.

Because of these issues, fits to the SEDs of high redshift quasars are unsuccessful using conventional quasar templates plus those for typical normal (e.g., \sim solar metallicity) SF galaxies, a method that works well for low-to-intermediate redshift quasars (e.g., Mullaney et al. 2011; Magdis et al. 2013; Xu et al. 2015b). In this paper, we demonstrate that the SEDs of $z \gtrsim 5$ quasars can be modeled using a moderately low-metallicity galaxy template to represent the AGN host galaxy. We combine a galaxy template derived from Haro 11 and a modified AGN template based on Elvis et al. (1994) to provide physically-motivated fits that successfully reproduce these $z \gtrsim 5$ quasar infrared SEDs. This simple model can be used to probe the relation between the AGN activity and host star formation in quasars with very limited observations.

Throughout this paper, we adopt cosmology $\Omega_m = 0.27$, $\Omega_\Lambda = 0.73$ and $H_0 = 71 \text{ km s}^{-1} \text{ Mpc}^{-1}$.

2. SELECTION OF SED TEMPLATES

In modeling the SEDs of quasars at $z \gtrsim 5.0$, the dearth of data points at long wavelengths requires minimizing the number of free parameters in SED fitting. While more precise fittings may be achieved by adding more free parameters, the scientific interpretation is then more subject to model degeneracy. To first order, the SED of a quasar should consist of an AGN component, and a host galaxy component. If suitable SED templates can be found, we only need two free parameters to normalize their contributions. Such a two-parameter model can be used to retrieve information from sources with less complete observations and make the interpretation less ambiguous.

2.1. Host Galaxy Template: Why Haro 11?

Galaxies at $z \sim 2 - 3$ are of relatively low-metallicity (e.g., Cullen et al. 2014; Maier et al. 2014). Confirming the trend toward lower metallicity to $z \gtrsim 5$ is difficult with current capabilities. Recently, some groups have tried to detect the dust continua of $z > 6$ normal galaxies using the Atacama Large Millimeter/Submillimeter Array (ALMA). The unexpected failures of almost all of these efforts have led to the interpretation that these $z > 6$ galaxies may be scaled-up versions of local very metal-poor dwarf galaxies (e.g., Ouchi et al. 2013;

Maiolino et al. 2015). As Fisher et al. (2014) pointed out, it would be almost impossible to observe the dust emission of any $z > 6$ galaxies with extreme low metallicity like the local dwarf galaxy 1 Zw 18. For the most luminous systems, however, the change in metallicity seems to be modest (e.g., Rawle et al. 2014). As a result, the ideal sample to draw a representative template for IR observable high- z galaxies is the moderately low-metallicity galaxies in the local Universe.

In addition, AGN host galaxies at $z > 4$ are found to be compact with typical sizes $\sim 1\text{-}3$ kpc, from observations at rest-frame UV (Jiang et al. 2013), deep K_s -band images (Targett et al. 2012), dust continuum maps (Wang et al. 2013), submm fine structure line maps (e.g., Wang et al. 2013; Willott et al. 2013, 2015), molecular gas distributions (e.g., Walter et al. 2004, 2009; Wang et al. 2013), and from SED analysis (Greve et al. 2012). Compared with extended galaxies of the same infrared luminosity, they are expected to have hotter far-IR SEDs due to compact star forming regions (Groves et al. 2008). Thus, we are motivated to search for a moderately low-metallicity galaxy with a high surface density of star formation to provide a SED analogous to that we expect for the star formation in the host galaxies of high- z quasars.

Appendix A presents the procedure to derive low-metallicity galaxy templates. To summarize briefly, we began with the sample of the Dwarf Galaxy Survey (DGS; Madden et al. 2013), which includes the largest metallicity range observable in the local Universe, with $12+\log(\text{O}/\text{H})$ ranging from 7.14 to 8.43, and spans four orders of magnitude in star formation rates. Combining their *Herschel* far-IR data (Rémy-Ruyer et al. 2013) and archival WISE mid-IR photometry, we fit the broad-band SEDs with a far-IR modified blackbody plus a mid-IR power-law component, and replaced the mid-IR fit SEDs with the corresponding *Spitzer* spectra. Among the 19 dwarf galaxies studied in detail, Haro 11 is the best candidate analog for high- z galaxies. Haro 11 is a moderately low-metallicity ($Z = 1/3 Z_\odot$, James et al. 2013) dwarf ($M_* = 10^{10} M_\odot$, Östlin et al. 2001) galaxy in the nearby Universe ($D = 92.1$ Mpc, Bergvall et al. 2006). It shows substantial star formation activity ($\text{SFR} \approx 20 - 30 M_\odot/\text{yr}$, Grimes et al. 2007, see also Appendix B.2) and emits strongly in the infrared ($L_{\text{IR}} \approx 2.0 \times 10^{11} L_\odot$, Adamo et al. 2010). Haro 11 also contains an extremely young stellar population with age < 40 Myr (Adamo et al. 2010). Some authors suggest it is a local analogue of the high- z Lyman break galaxies (LBGs) or Lyman- α emitters (Hayes et al. 2007; Leitert et al. 2011).

Besides low metallicity, the most important two features of Haro 11 are its high star formation rate and compact size, indicating a very high star formation surface density. From our estimation, the star formation rate of Haro 11 can be as high as $\sim 32 M_\odot/\text{yr}$ (based on L_{IR} and L_{FUV} , see Appendix B.2), which is significantly higher than the vast majority of dwarf galaxies in the literature (Hopkins et al. 2002). Meanwhile, Haro 11 has a compact size. Its MIPS $24\mu\text{m}$ image is perfectly diffraction-limited (see Figure 1), which puts an upper-limit on its IR emitting region size ($< 3.4''$ or 1.2 kpc). The size of the star formation region of Haro 11 con-

strained from high-resolution $H\alpha$ images (Östlin et al. 2009) is also small (~ 1.3 kpc from measuring 50% total flux, and ~ 2.7 kpc from measuring 90% total flux). The IR luminosity surface density, $\Sigma_{L(\text{IR})}$, of Haro 11 is $\sim 10^{11} L_{\odot}/\text{kpc}^2$, which approaches the values in galaxies at $z \gtrsim 4$ (e.g., GN20 has $\Sigma_{L(\text{IR})} \sim 10^{12} L_{\odot}/\text{kpc}^2$, Hodge et al. 2015). The high star formation rate surface density and infrared luminosity surface density of Haro 11 are exceptional among dwarf galaxies, making it the most suitable local analog to high- z quasar host galaxies.

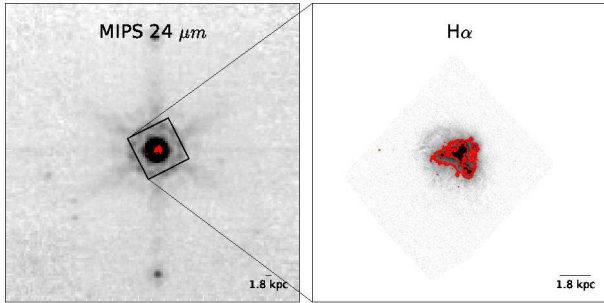


FIG. 1.— The *Spitzer* MIPS $24\mu\text{m}$ (left; Program ID: 59, PI: G. H. Rieke) and the HST $H\alpha$ (right; Östlin et al. 2009) images of Haro 11. The $H\alpha$ image is zoomed to view the central square region on the $24\mu\text{m}$ image. We also overplot the same $H\alpha$ contours (red lines) on both images.

In Figure 2, we compare the derived Haro 11 template with a number of normal solar-metallicity star-forming (SF) templates in Rieke et al. (2009). Haro 11 has a larger mid-IR slope with $\alpha = 3.63$ ($f_{\nu} \propto \lambda^{\alpha}$), in contrast with normal galaxies with $\alpha \sim 2.0$ (e.g., Blain et al. 2003; Casey 2012). The derived dust temperature is $T = 46.5$ K with emissivity index $\beta = 1.9$. Haro 11 also presents very weak aromatic features compared with normal galaxies. All these characteristics are commonly seen for other dwarf galaxies (see Appendix A.3). Compared with the Rieke et al. (2009) SED templates with $\log L_{\text{IR}} < 11.50$, which are representative for $z \sim 2$ galaxies (see Section 3.1), Haro 11 has similar L_{IR} surface densities but higher dust temperature. We suggest the low-metallicity of Haro 11 is the most likely reason for its warmer SED.

2.2. AGN Continuum Template

Candidate AGN templates can be derived from either numerical models (e.g., Fritz et al. 2006; Hönig & Kishimoto 2010) or semi-analytic models (e.g., Mullaney et al. 2011; Sajina et al. 2012). However, such models always have many free parameters, which need to be optimized to fit real AGN behavior. Hence the starting point for determining AGN templates needs to be an accurate empirical version.

Elvis et al. (1994) built an X-ray to radio SED template for a sample of 47 well-defined optically selected quasars and subtracted the host galaxy emission in the UV/optical and near-IR bands. This template has become the classic representation of Type 1 AGN SEDs in the ultraviolet, visible, near, and mid-infrared. Many studies based on larger samples and modern data have closely reproduced the Elvis

template (e.g., Richards et al. 2006; Shang et al. 2011; Runnoe et al. 2012; Elvis et al. 2012; Hanish et al. 2013; Scott & Stewart 2014). The remarkable similarity of these results to the Elvis template is demonstrated by the comparisons in Scott & Stewart (2014) (their Figure 5). The success of the Elvis template is also demonstrated by its broad application, for example, to study the SEDs of type-1 AGN in XMM-COSMOS (Elvis et al. 2012) and decompose the SEDs of intermediate-redshift quasars in Xu et al. (2015b). The template shape appears to vary little with cosmic evolution or other characteristics such as the Eddington ratio (e.g., Hao et al. 2011, 2014). In particular, this template appears to work equally well to $z \sim 6$. Jiang et al. (2006) demonstrated that the rest-frame $0.15 - 3.5\mu\text{m}$ SEDs of 13 $z \sim 6$ quasars can be matched with the Elvis et al. (1994) template. Wang et al. (2008b) demonstrated that the average optical-to-near-IR SED of 33 $z \sim 6$ quasars is consistent with the Elvis template. Jiang et al. (2010) find that the near infrared and optical-to-NIR colors of hundreds of quasars are virtually the same from the local epoch to $z \geq 6$, i.e., they are consistent with a common SED shape, which must therefore be consistent with the Elvis template. Therefore, the Elvis template is a useful metric for testing more complex models and is currently the most suitable approach for SED decompositions involving UV-luminous Type-1 AGNs.

There are two issues in applying the Elvis template. The first is that it is likely to have a residual contribution in the far infrared from dust heated by star formation, a possibility that has hindered its application in using the far infrared to measure star formation rates in quasar host galaxies (e.g., Barnett et al. 2015). However, a version of the template corrected for this effect is now available (Xu et al. 2015b). Based on the analysis of the *Spitzer* and IRAS data of the Elvis et al. (1994) sample, these authors found a tight correlation between the strength of the $11.3\mu\text{m}$ aromatic feature and the infrared 60 to $25\mu\text{m}$ flux ratio. They concluded that star formation, as traced by the aromatic feature, boosted the infrared flux ratio in the template by a factor of 1.27. A scaled Rieke et al. (2009) star-forming galaxy template ($\log L_{\text{IR}} = 11.0$) was subtracted from the Elvis et al. (1994) template to remove this contribution. The second issue is that of order 10% of quasars have SEDs similar to the Elvis template in the UV and optical, but are relatively weak in the near and mid-infrared, a behavior attributed to a relative lack of hot dust (Hao et al. 2010, 2011). The exact SED shape of these dust-poor quasars requires future work to address.

Leipski et al. (2013) used three components to represent the AGN SEDs for their high redshift quasar sample: a UV/optical power-law, a NIR dust emission component, and a torus model. They adjusted the relative contributions of these components to optimize their SED fits. However, all three components are implicitly embedded in the Elvis template. Any adjustments in relative strengths should only be made after it has been demonstrated that the Elvis template (or similar ones) gives an unsatisfactory fit. In this work, we use the Elvis template for our SED decomposition. When combined with the Haro 11 template, we find that its fits are of comparable quality to the relatively unconstrained fits used by Leipski et al. (2013, 2014) in the sense of chi-square tests.

There is thus no advantage for our study in using those more complex and less constrained models for the quasar SEDs - they introduce additional free parameters without improving the fits correspondingly (see Section 3.3).

2.3. Fitting Procedure

To compare the templates described above to observations, we used a fitting procedure that takes into account upper-limit data points where available. For n measurements of x_i with uncertainties σ_i and m non-detections with $x_j < n\sigma_j$ (n^{th} confidence level), we define the fitting chi-square as (Isobe et al. 1986):

$$\chi_{\text{total}}^2 = \sum_i^n z_i^2 - \sum_j^m 2 \ln \frac{1 + \text{erf}(z_j/\sqrt{2})}{2}, \quad (1)$$

where

$$z_i = \frac{x_i - \hat{x}_i(\theta)}{\sigma_i}, \quad (2)$$

$$\text{erf}(x) = \frac{2}{\sqrt{\pi}} \int_0^x e^{-t^2} dt, \quad (3)$$

which is the error function, and $\hat{x}_i(\theta)$ is the modeled value. In Equation 1, the first term on the right-hand side is the classical definition of chi-square, and the second term introduces the error function to quantify the fitting of upper-limits. We use Markov Chain Monte Carlo (MCMC) methods to find the parameter set θ to minimize χ_{total}^2 . 3σ upper limits are adopted for all non-detections. To compare the fitting quality of different fitting methods, the total χ_{total}^2 should be normalized by the degrees of freedom, ν . In our case, $\nu = n + m - k$, where k is the number of free parameters in the model. We will use χ_{ν}^2 to represent the reduced chi-square, i.e., $\chi_{\nu}^2 = \chi_{\text{total}}^2/\nu$.

To deal with the trade-off between the goodness of fit and the complexity of the model, we use the corrected Akaike Information Criterion (AICc) test (Sugiura 1978), which is defined by

$$\text{AICc} = -2 \ln \mathcal{L}_{\text{max}} + 2k + \frac{2k(k+1)}{N - k - 1}, \quad (4)$$

where \mathcal{L}_{max} is the maximum likelihood achievable by the model, and N is the number of data points used in the fit, $N = n + m$. The likelihood of a model to fit data satisfies

$$-2 \ln \mathcal{L}_{\text{max}} = \chi_{\text{total}}^2 + C, \quad (5)$$

where the constant C is related to the errors, σ_i , and the binning, Δx_i , of the data points, which are fixed at the time of observations. We can ignore C when comparing different models to fit the same observations, and finally have

$$\text{AICc} = \chi_{\text{total}}^2 + 2k + \frac{2k(k+1)}{n + m - k - 1}. \quad (6)$$

3. TESTS OF THE TEMPLATES

3.1. Template Fits for High- z Galaxies

We now discuss alternative SF template candidates to be used at high- z . Rieke et al. (2009) derived templates for local normal star-forming galaxies with different infrared luminosities (L_{IR}). Although carefully

calibrated in the local Universe, these templates may not apply at high redshift. The star formation in luminous galaxies at high- z has been found to be more physically extended than that in local galaxies with similar L_{IR} (local LIRGs and ULIRGs are sub-kpc, whereas high- z DSFGs are kpc in size, see Rujopakarn et al. 2011). Rujopakarn et al. (2011, 2013) found that the Rieke et al. (2009) $\log L_{\text{IR}}=11.00-11.50$ SED templates are representative of galaxies found at $0.4 < z < 2.7$ due to their similar L_{IR} surface densities. This argument is supported by the consistency between the empirical average SED of $z \sim 2$ galaxies derived in Kirkpatrick et al. (2012) and the $\log L_{\text{IR}}=11.00-11.50$ SED templates from Rieke et al. (2009) (Figure 3). In fact, Figure 3 shows the progressively poorer correspondence of the Rieke et al. (2009) templates with the empirical one with increasing L_{IR} . It is also consistent with the finding of a shift toward colder FIR SEDs at high redshift by Symeonidis et al. (2009, 2013). Greve et al. (2012) found evidence of extended structures in DSFGs out to redshift $z \sim 4.0$, based on analysis of their infrared SEDs. With this evidence, we focus on Rieke et al. (2009) SED templates with luminosity $\log L_{\text{IR}} < 11.50$ in the following comparisons. These normal SF templates represent galaxies that are almost certainly more metal-rich than is appropriate for $z > 4$. We will therefore compare them with fits using a template derived from Haro 11.

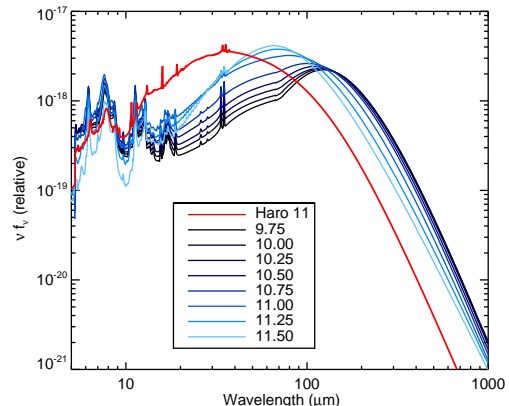


FIG. 2.— Comparison of Haro 11 template (red line) and the normal star-forming galaxy templates with $\log L_{\text{IR}} = 9.75 \sim 11.50$ in Rieke et al. (2009) (blue lines). All the templates are normalized to have the same $L_{\text{IR,template}}$

We test the Rieke et al. (2009) and Haro 11 template fittings to extremely high- z galaxies, as examples of potential host galaxies for high redshift quasars. Due to the lack of data available for star-forming galaxies at $z > 5$, we extend our redshift range down to $z = 4$. We find 8 galaxies (see Table 1) with multiple constraints on their rest-frame infrared SEDs, suitable for comparison with these templates. By selection, these highest- z DSFGs are limited to a handful of submillimeter galaxies (SMGs), which were originally discovered in the submm and relatively bright in the far-IR. The identification technique of SMGs could bias their SEDs to be relatively cold compared with high- z galaxies selected in other ways (Le Floc'h et al. 2004), whereas the SEDs of low-metallicity galaxies tend to be relatively hot (e.g.,

TABLE 1
COMPARISONS OF GALAXY TEMPLATES USED TO FIT $z > 4$
GALAXIES

Source (1)	z (2)	$\chi^2_{\nu, \text{Haro11}}$ (3)	R09 best (4)	$\chi^2_{\nu, \text{R09}}$ (5)	Ref. (6)
HFLS 3	6.34	13.1	11.50	30.9	1
AzTEC 3	5.30	1.5	11.50	2.3	2, 3
HLS J0918+5142	5.24	18.1	11.50	18.4	3
AzTEC 1	4.64	6.9	11.50	2.0	3
Capak4.55	4.55	0.6	11.50	2.1	3
ID 141	4.24	5.7	11.50	17.9	5
GN10	4.05	3.2	11.50	1.5	3
GN20	4.05	23.1	11.25	0.2	3

NOTE. — Col. (1): Source names sorted by their redshifts; Col. (3): χ^2_{ν} of Haro 11 template fitting; Col. (4): the Rieke et al. (2009) template which has the minimum χ^2_{ν} ; Col. (5): minimum χ^2_{ν} among tested Rieke et al. (2009) templates; Col. (6): references for photometric data.

References. (1) Riechers et al. (2013); (2) Dwek et al. (2011); (3) Huang et al. (2014); (4) Rawle et al. (2014); (5) Cox et al. (2011)

Rémy-Ruyer et al. 2013). As a result, the high- z galaxy examples studied here might be biased against typical low metallicity galaxies, which, as in the case of Haro 11, tend to have SEDs dropping rapidly toward the submm.

Table 1 summarizes the fitting results for the $z > 4$ galaxies. We limit the fits to rest-frame 8-1000 μm , where the emission is purely from dust. Although a few examples, e.g., GN20, have a cold far infrared SED matched better by the Rieke et al. (2009) templates, in general the fits with the Haro 11 SED are at least as good. We conclude that it is as good as the local higher metallicity templates in fitting the SEDs of these extreme $z > 4$ SMGs. That is, even given the selection bias against it, the Haro-11-based template can be used without a substantial loss of accuracy.

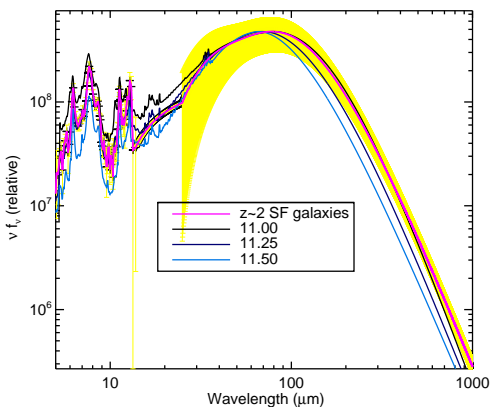


FIG. 3.— Comparison of the $z \sim 2$ galaxy SED in Kirkpatrick et al. (2012) (magenta line with template errors in yellow) and the normal star-forming galaxy templates with $\log L_{\text{IR}} = 11.00, 11.25, 11.50$ in Rieke et al. (2009) (black, navy, blue lines). All the templates are normalized to have the same $L_{\text{IR, template}}$

3.2. Template Fits for High- z Quasars

The Elvis et al. (1994) template has been shown to match type-1 quasar SEDs for redshifts up to $z \sim 3$ and for wavelengths $\lambda \lesssim 24 \mu\text{m}$ (Hao et al. 2014; Xu et al.

2015b). An issue in applying it, or the similar template of Richards et al. (2006), in the far-IR is the uncertain contribution of host galaxy star formation (e.g., Barnett et al. 2015). However, Xu et al. (2015b) were able to correct for this effect. In Figure 4, we compare this corrected template with the stacked SEDs from Leipski et al. (2014). While the UV-to-optical parts of all three SEDs are well matched with the AGN continuum template, differences emerge in the infrared. The stacked SED of quasars detected in at least 3 *Herschel* bands has a substantial excess over the AGN template in the far-IR, which we attribute to host galaxy star formation (see Section 5.1). The stacked SED of quasars not detected with *Herschel* is not matched as well in the infrared although the reduced chi-square is still acceptable. This behavior could be due to the unsuitability of a classical AGN template to represent the hot-dust-free (Jiang et al. 2010) or hot-dust-poor (Hao et al. 2010, 2011) quasars (hereafter hot-dust-deficient quasars, or HDD quasars) as pointed out by Leipski et al. (2014). The fit to the *Herschel* partly-detected (detected in only 1-2 *Herschel* bands) stacked SED is virtually perfect over the entire wavelength range. The agreement of the template with both the *Herschel*-undetected and *Herschel* partly-detected stacked SEDs suggests that the star-formation corrected Elvis SED is a good choice to fit the high-redshift AGN continua. More discussion will be provided in Section 5

3.3. SED Fitting with Well-measured High- z Quasars

To test further whether the Haro 11 template as well as the AGN (modified Elvis et al. (1994)) template are reasonable choices to decompose $z \gtrsim 5$ quasar SEDs, we focus on 5 quasars with the most complete infrared SEDs. Besides SDSS J1204–0021, the SEDs of all the other quasars were studied in Leipski et al. (2013)³. We model the observed rest-frame 1-1000 μm SED as a linear combination of the Haro 11 template and the AGN template with two free normalizing factors. These two templates are taken to be independent. To compare the Haro 11 template with the normal SF templates, we replace the Haro 11 template by the normal SF templates in Rieke et al. (2009), and redo the fit. We also apply the Leipski et al. (2013) model to the UV-to-IR SED of these quasars and compare the fits of the IR SED with those from our two-component models.

In Figure 5, we present the SED decomposition results. In general, the Haro 11 template fits have smaller residuals ($\lesssim 0.3$ dex) compared with the best-fit⁴ normal SF template. In particular, the Haro 11 template yields much better fits in representing the warm dust component from the two-component decomposition. We comment on the two-component fits (left and middle columns

³ Among the five millimeter-detected quasars with at least two *Herschel* observations in Leipski et al. (2013), SDSS J1044–0125 is excluded since the number of detected data points at rest-frame 1 – 1000 μm is smaller than the number of free parameters of the Leipski et al. (2013) model. This hinders the computation of a reduced chi-square of the Leipski et al. (2013) model for only the IR data points to be compared with the two-component fits.

⁴ We fit these quasars with normal SF templates in Rieke et al. (2009) with $\log L_{\text{IR}} \leq 11.50$, and pick the one that has the lowest χ^2_{ν} as the best. The $\log L_{\text{IR}} > 11.50$ normal SF templates do not yield any better results, especially in the mid-IR, as shown in Figure 5.

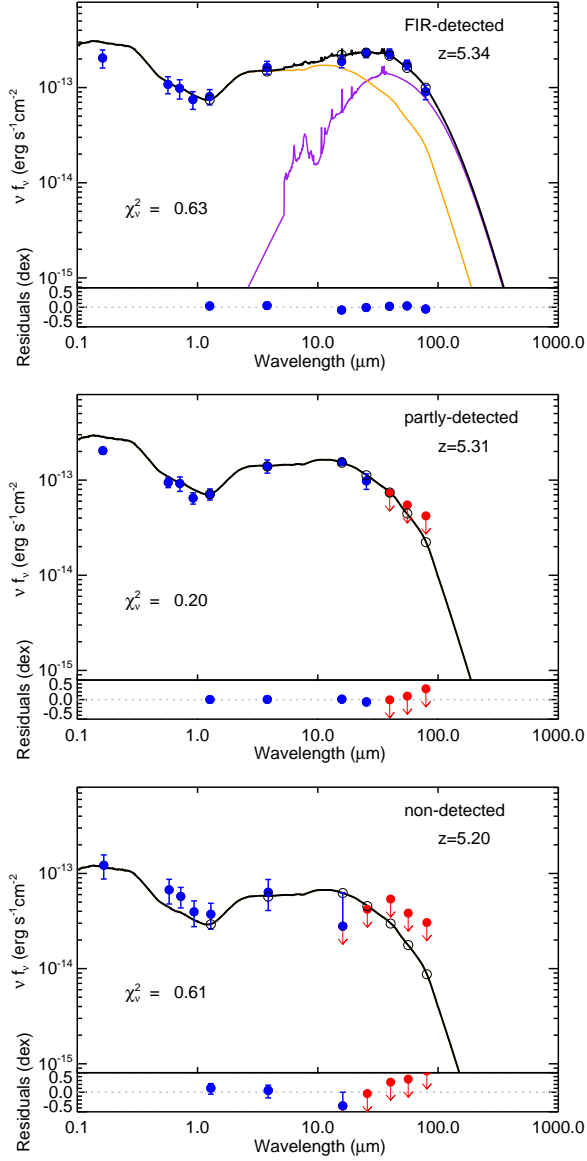


FIG. 4.— Three stacked SEDs in Leipski et al. (2014) and our fitting results. We limit the fitting to rest-frame wavelengths 1–1000 μm . The black solid line is the modelled SED, the black circles are the modelled points (convolved with the corresponding photometric filters). The AGN component and galaxy component are shown as gray and purple solid lines, respectively. The blue dots are for detections with 1σ error bars and red dots are for upper limits at 3σ . The reduced chi-square of the fit is shown on the bottom left of each plot.

of Figure 5) for each SED below:

J0338+0021 (or SDSS J033829.31+002156.3; we use JHHMM \pm DDMM for brevity). The Haro 11 template is better than the best normal SF template in decomposing the SED. Fitting the mid-IR at $< 10\mu\text{m}$ and the far-IR drop beyond $100\mu\text{m}$ results in the normal SF template model underestimating the flux at $10 - 100\mu\text{m}$. We note an excess between $\sim 10\mu\text{m}$ and $\sim 40\mu\text{m}$ over the normal SF template fitting model SED, which could be the warm excess seen in relatively low- z AGN SEDs reported by Xu et al. (2015b). In contrast, such an excess is not strong in the Haro 11 template fits.

J0756+4104. Judging from the fit χ^2_ν , the normal SF template seems better. However, $\sim 50\%$ of the χ^2_ν of the Haro 11 template fit is contributed by the data point at the longest wavelength ($\lambda_{\text{rest}} = 139\mu\text{m}$), whereas the χ^2_ν contribution of the same data point in the normal SF template fitting is minimal. Again, the normal SF template fitting underestimates the SED at $\sim 10 - 40\mu\text{m}$. We conclude the normal SF template and the Haro 11 template yield fits of similar quality.

J0927+2001. The Haro 11 template is much better than the normal SF template in reproducing the observed SED. The maximum deviation of the dwarf galaxy model and observed SEDs is less than 0.3 dex. In the case of this quasar, the normal SF template underestimates the SED at $\sim 10 - 100\mu\text{m}$.

J1148+5251. For this well-studied quasar, the Haro 11 template fitting is almost the same as the best normal SF template fitting when comparing χ^2_ν . Interestingly, our estimation of the host contribution of this quasar is consistent with result based on the theoretical analysis by Schneider et al. (2014).

J1204-0021. This is the only case where the Haro 11 template fitting has one data point with fitting residual (slightly) greater than 0.3 dex. Both two-component fits underestimate the observed $10 - 100\mu\text{m}$ flux. However, the residual from the Haro 11 template fitting is much smaller than the normal SF one.

For the Leipski et al. (2013) model (right column of Figure 5), we only apply the fit to the detected data points in the UV-to-IR, in the same fashion as Leipski et al. (2013), and compute the χ^2_ν for the detected data points at rest-frame 1–1000 μm . Since it has more components, especially a torus component selected from a large model library, small details of the observed SED can be reproduced. Thus, the residuals are generally smaller. However, our two-parameter fit has similar reduced chi-square compared with the Leipski et al. (2013) model, despite its simplicity. To judge which fit is preferred, we have used the AICc test (see Section 2.3). Since the slope of the power law component is not useful in fitting the infrared data, we have assumed that the Leipski et al. (2013) fits had six free parameters over 1–1000 μm . As shown in Table 2, the value of AICc is lower in all five cases for the 2-parameter fits, indicating that they are indeed preferred. That is, even for these quasars with the maximum number of measurements, the Leipski et al. (2013) model over-fits the data compared with our two-parameter one.

In summary, we find that the Haro 11 galaxy template and the modified Elvis AGN template are at least as good at fitting the overall high- z quasar SEDs as the fits using templates for local star forming galaxies of solar metallicity. The Haro 11 template fits better in the rest-frame mid-IR, but may be slightly worse in the far-IR range. Though the Leipski et al. (2013) model could reproduce more details of the observed SED, our two-component model yields fits of comparable overall quality and is preferred in model selection due to its simplicity.

4. AGN AND HOST GALAXY DECOMPOSITION FOR QUASARS AT $Z \gtrsim 5$

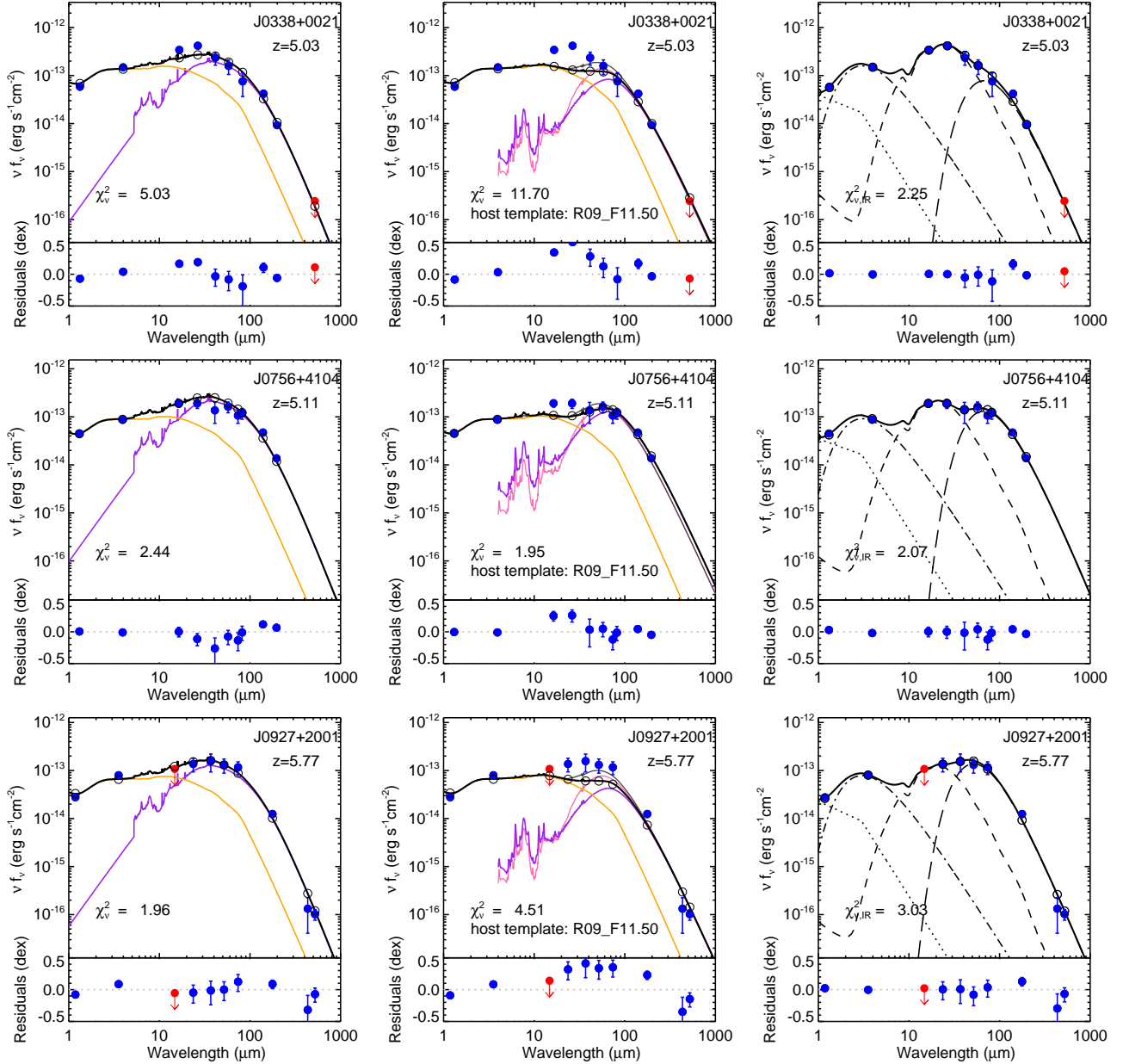


FIG. 5.— SEDs and their decompositions for 5 quasars with strong far-IR SED constraints. The plots show νF_ν in units of erg/s/cm^2 over the rest-frame wavelengths. We show the results from “Haro 11 + AGN” decomposition (left column), “normal SF galaxy + AGN” decomposition (middle column), and the Leipski et al. (2013) model (right column). In each plot, the blue dots are for detections with 1σ error bars and red dots are for upper limits at 3σ . The bottom panel of each plot presents the residuals from the fit. In the left and middle columns, the colored lines show the results of a two-component SED fit as described in Section 2: the SF-subtracted type-1 AGN template in orange, and a galaxy template in purple. The black line is the total of these two components. The black circles are the synthetic photometry points from the model. To demonstrate that Rieke et al. (2009) templates with $\log L_{\text{IR}} > 11.50$ do not yield better results, we make another fitting with Rieke et al. (2009) $\log L_{\text{IR}}=12.50$ template, and plot the fitted galaxy component (pink thin line) and the total model SED (gray thin line) in the middle column. In the right column, we use the Leipski et al. (2013) model, which is a combination of a UV/optical power-law (dotted line), a 1200 K near-IR dust component (dot-dashed line), a near-/mid-IR torus model (short-dashed line), and a modified black-body far-IR component with $\beta = 1.6$ (long-dashed line).

Combining *Herschel*, *Spitzer* and ground-based 250 GHz observations, we apply the “Haro 11 + AGN” two-component fit to the observed SEDs of all 69 quasars in Leipski et al. (2014) (hereafter, *sample-A*). Since our interest is the infrared output, we again limit the fit to rest-frame $1.0 - 1000\mu\text{m}$. The fits are presented in Figure 6. We can confirm again the suitability of the modified Elvis et al. (1994) AGN template: the near-IR to mid-IR SEDs of these $z \gtrsim 5$ quasars are well-matched

with our empirical AGN template in 58 cases. Combining with the Haro 11 template, this modified Elvis et al. (1994) AGN template provides reasonably good fittings to all these $z \gtrsim 5$ quasars, which suggests the Elvis et al. (1994) AGN template derived on local quasars is suitable for vast majority of $z \gtrsim 5$ quasars. There are 11 cases where the Elvis template overestimates the mid-infrared, which is the signature of HDD quasars: the incidence of this behavior ($\sim 16\%$) is similar to that observed at lower

TABLE 2
SED DECOMPOSITION RESULTS FOR $z \geq 5.5$ QUASARS WITH WELL-MEASURED SEDS

Source (1)	Redshift (2)	$L_{\text{IR}}/10^{13} L_{\odot}$ (3)	$f_{\text{host,IR}}$ (4)	χ^2_{ν} (5)	AICc (6)	R09 best (7)	$\chi^2_{\nu, \text{R09}}$ (8)	$\chi^2_{\nu, \text{L13,IR}}$ (9)	AICc _{L13} (10)
SDSS J0338+0021	5.03	4.01	0.57	5.03	45.95	11.50	11.70	2.25	49.00
SDSS J0756+4104	5.11	3.77	0.69	2.44	25.26	11.50	1.95	2.07	48.28
SDSS J0927+2001	5.77	3.21	0.64	1.96	21.39	11.50	4.51	3.03	52.12
SDSS J1148+5251	6.43	5.31	0.34	3.09	33.31	11.50	3.00	3.63	51.10
SDSS J1204−0021	5.03	3.79	0.46	6.92	54.44	11.50	14.91	18.78	110.34

redshift (Mor & Trakhtenbrot 2011). The χ^2_ν , derived total infrared luminosities ($L(\text{IR})$), and host component contributions from the fits are listed in Table 3. We also calculate the star formation rates using the method described in Section 5.3

We can compare the results of the host galaxy far-IR luminosity with other works. It is frequently assumed that the far-IR SED of high- z quasars can be described as a $T = 47$ K and $\beta = 1.6$ modified black body (Beelen et al. 2006) and the infrared luminosity of this component is used to estimate their star formation rates (e.g., Omont et al. 2013; Leipski et al. 2013, 2014; Calura et al. 2014; Willott et al. 2015). However, real galaxies have strong mid-infrared emission that is

under-represented by a single (modified) black body SED (e.g., Dunne & Eales 2001; Willmer et al. 2009; Galametz et al. 2012; Kirkpatrick et al. 2012). With the inclusion of the mid-IR energy contribution from star formation, the Haro 11 template yields an infrared luminosity $L_{\text{SF,IR}}$ 1.5-2.0 times larger than the infrared luminosity of the Beelen et al. (2006) modified black body template L_{FIR} , depending on the exact far-IR constraints to the galaxy component. Compared with the Leipski et al. (2014) results from the four-component decomposition on 19 quasars with most complete IR SED observations, our results are different, especially for the host galaxy far-IR luminosity. For a quasar with strong host galaxy far-IR emission, its mid-IR emission will be dom-

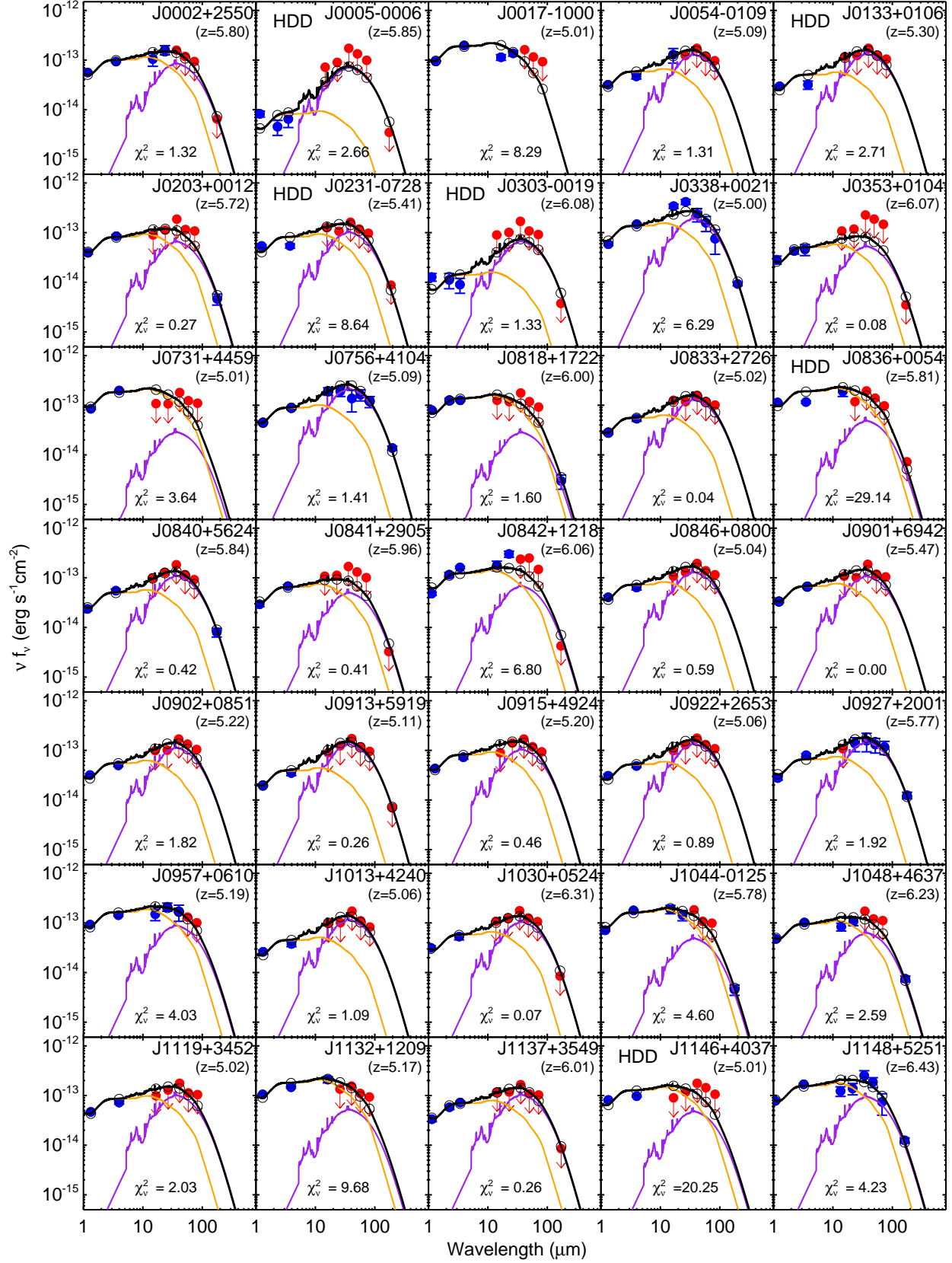


FIG. 6.— Two-component SED decompositions of 69 quasars (*sample-A*) in Leipski et al. (2014). The plots show νF_ν in unit of erg/s/cm^2 over the rest-frame wavelength. The black solid line is the modelled SED, the black circles are the modelled points. The AGN component and galaxy component are shown as gray and purple solid lines, respectively. The blue dots are for detections with 1σ error bars and red dots are for upper limits at 3σ . The reduced chi-square of the fit is shown on the bottom of each plot. We put a tag ‘HDD’ near the top-left corner of the panel if the corresponding quasar is identified as hot-dust-deficient (HDD).

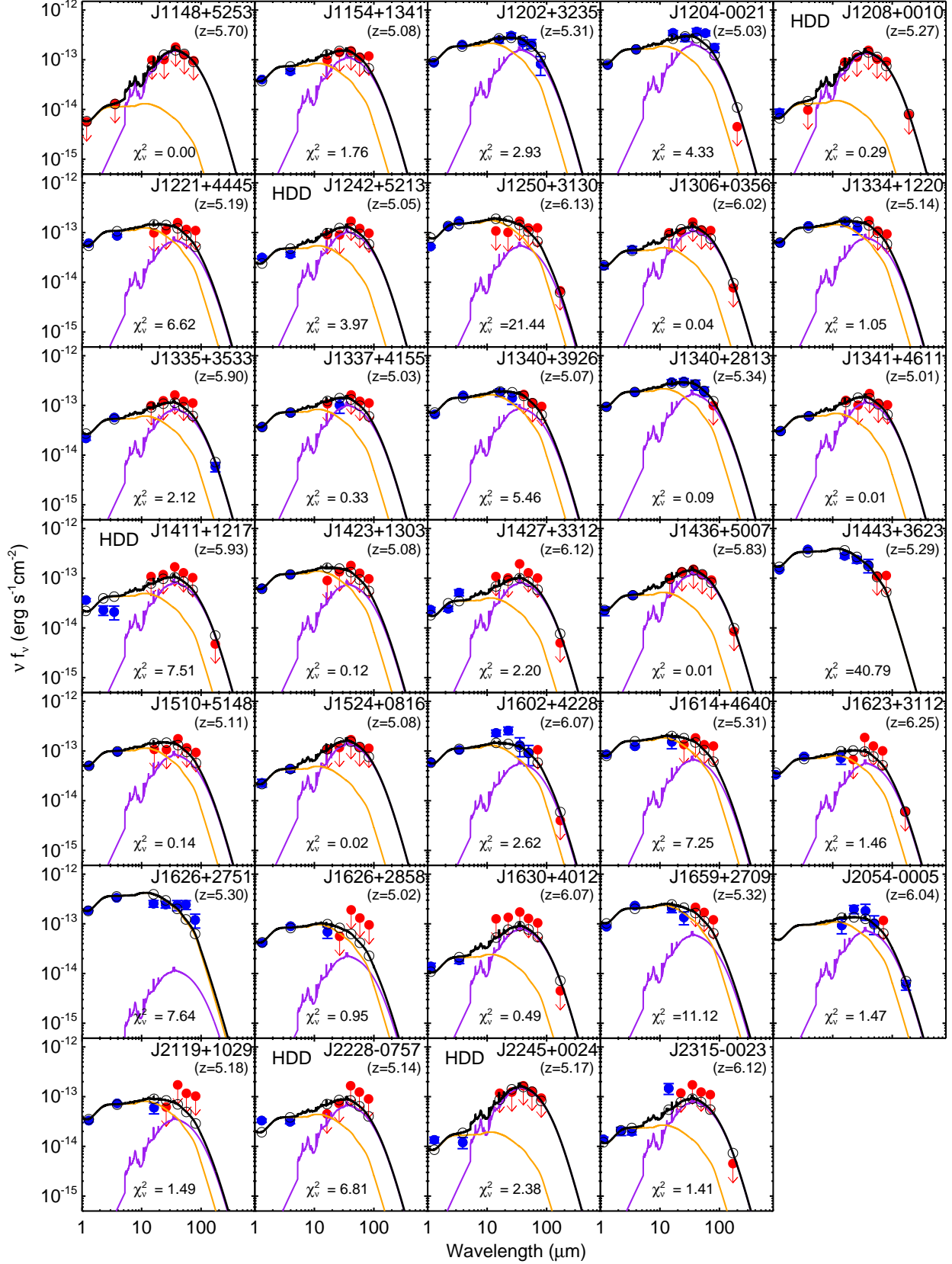


FIG. 6.— continued. Two-component SED decomposition of 69 quasars (*sample-A*) in Leipski et al. (2014).

inated by star formation. Since the modified black body misses significant luminosity at shorter wavelengths, the Leipski et al. (2013) model has to scale up the torus component to fit the rest-frame mid-IR data, ending with an overestimated fraction of the far-IR emission due to the AGN (the torus) and an underestimated host galaxy contribution. Consequently, the star formation rates derived by the Leipski et al. (2013) model in such cases (like SDSS J0756+4104, J0927+2001, J1202+3235, J1340+2813, which have $L_{\text{SF,IR}} \sim 2.2 - 2.9 L_{\text{FIR}}$) are much lower than our values. For a quasar without strong host galaxy far-IR emission, however, the Leipski et al. (2013) model gives a higher L_{FIR} than our $L_{\text{SF,IR}}$. Examples are SDSS J0842+1218, J1044-0125, J1048+4637, J1148+5251, J1659+2709, with $L_{\text{SF,IR}} \sim 0.5 - 1.0 L_{\text{FIR}}$. This discrepancy is still due to the template differences. The torus templates used in Leipski et al. (2013, 2014) by themselves generally underpredict the far-IR emission compared with our AGN template. As a result, the far-IR modified black body has to be scaled up to match the far-IR observations. We believe the star formation rate based on the $L_{\text{SF,IR}}$ from our model is more reliable, since 1) the host galaxy template is based on a real galaxy that includes the mid-IR star formation contribution; 2) the relative contributions of the torus and near-IR component are fixed in our AGN template that is based on real observations. In addition, thanks to the simplicity of the two-component model, we can place constraints on the host galaxy star formation for the other 50 $z \gtrsim 5$ quasars in Leipski et al. (2014), which only have upper-limits for the MIR-FIR SEDs and the Leipski et al. (2013) model can not fit. We will discuss our model results in Section 5.

We also searched for other $z \gtrsim 5.0$ quasars with rest-frame far-IR observations in the literature and found 33 more quasars not included in Leipski et al. (2014) (hereafter *sample B*). The majority of them have been listed in Calura et al. (2014), except for RD J0301+0020 and TN J0924-2201. We collected all available observations on dust continuum as well as the UV/optical continuum (Bertoldi & Cox 2002; Petric et al. 2003; Wang et al. 2008b, 2011b,c, 2013; Omont et al. 2013; Willott et al. 2013, 2015; Barnett et al. 2015). Because of the lack of constraints on the near-IR and mid-IR bands, we did not make full fits as for the cases in *sample-A*, but scaled the templates to some specific data points. For the AGN component, considering the potential extinction effect and possible lack of hot dust emission (to be discussed in Section 5), we scale the template to the data point at $\lambda_{\text{rest}} = 0.1450 - 1.0 \mu\text{m}$, which yields a maximum AGN luminosity. For the host component, we scale the Haro 11 template to the data point at $\lambda_{\text{rest}} > 50 \mu\text{m}$, which yields a minimum IR luminosity. Then we calculated their total infrared luminosities, the fraction of host contribution, and star formation rates, as summarized in Table 4. Compared with *sample-A*, *sample-B* contains less-luminous quasars (mainly contributed by the Canada-France High- z Quasar Survey, see Omont et al. 2013 and references therein), and consists almost entirely of quasars at $z > 5.7$.

In the following discussion, we will mainly focus on *sample-A*, whose data points are more uniformly collected and have the same detection limits. We will discuss *sample-B* only as a complement to conclusions based

on *sample-A*.

5. DISCUSSION

5.1. Heating Sources for the Infrared Energy Output

To study the host galaxies of high- z quasars from infrared SEDs, the heating sources of the infrared-emitting dust and the contribution from the host star formation should be examined first. Previously, a number of papers made the assumption that the heating process for the FIR-emitting warm dust is dominated by host star formation (e.g., Leipski et al. 2014), or assumed some conservative fraction of host star formation heating (e.g., Wang et al. 2011c). From a theoretical point of view, Li et al. (2008) and Schneider et al. (2014) studied the heating of the observed SED of J1148+5251, an archetypal high-luminosity high-redshift quasar. They argued that the heating of the dust in the host galaxy could be dominated by processes related to the central engine, rather than the host star formation. This field is quite controversial.

As shown in Figure 6, the AGN template from Xu et al. (2015b) is not sufficient to reproduce the far-IR SED of many $z \gtrsim 5$ quasars with rest-frame far-IR detections. To investigate the average infrared properties of these quasars, we fit the three stacked SEDs in Leipski et al. (2014), shown in Figure 4. For the FIR-detected SED (from objects detected at least three *Herschel* bands), we can see a clear contribution in the far-IR from the host galaxy. For the partly detected SED (from objects with significant PACS 100 μm and/or 160 μm flux), the AGN template alone is enough to reproduce the SED. For the objects without any *Herschel* detections, there are some HDD quasars with SEDs deviating from normal AGNs, as indicated by the low ratio of rest 24 μm to optical. The stacked SEDs for the 14 partly *Herschel* detected and the 33 non-detected systems show no evidence for significant far-IR output over that of typical quasar templates. It would be difficult to understand why just 10 of this sample had strong heating of the host galaxy ISM by the quasar. A plausible explanation is that these 10 *Herschel*-detected systems have high levels of star formation, while for the other quasars the star formation is weak.

At very high redshift, cosmic microwave background (CMB) is also a source for dust heating (da Cunha et al. 2013). However, since the dust temperatures in high- z quasar host galaxies are typically $\sim 35\text{--}50\text{K}$ (e.g., Xu et al. 2015b; Leipski et al. 2014), at least twice the CMB temperature for the relevant redshift range ($T_{\text{CMB}} \sim 18\text{K}$ at $z \sim 5.5$), a correction is not significant compared with the other uncertainties in our derivations.

5.2. Are AGN Host Galaxies at $z \gtrsim 5$ Low-metallicity?

For quasars at $z \sim 1 - 6$, emission line ratios are found to trace (super-)solar gas metallicities (up to $\sim 10 Z_{\odot}$) in broad line regions (BLRs) without any strong indication of redshift evolution (Nagao et al. 2006, 2012; Jiang et al. 2007; Juarez et al. 2009). However, the mass of the BLRs is small ($10^2 - 10^4 M_{\odot}$), and might not be representative of the overall formation history of the galaxy. Wang et al. (2010a, 2011a) showed that the star formation can be enhanced in the accretion flow of the AGN, possibly resulting in locally increased metallicity.

TABLE 3
SED DECOMPOSITION RESULTS FOR $z \gtrsim 5.0$ 69 QUASARS (*sample-A*)

Source (1)	z (2)	$m_{1450\text{\AA}}$ (3)	χ^2_ν (4)	$L_{\text{IR}}(10^{13}L_\odot)$ (5)	$f_{\text{host,IR}}$ (6)	c_{SFR} (7)	$\text{SFR}(M_\odot/\text{yr})$ (8)
SDSS J000239.39+255034.8	5.80	19.0	1.32	≤ 3.18	≤ 0.44	0.88	≤ 2394
SDSS J000552.34-000655.8*	5.85	20.8	2.66	≤ 1.34	≤ 0.89	0.61	≤ 1408
SDSS J001714.67-100055.4	5.01	19.4	8.29	≤ 2.39	≤ 0.00	1.00	$\leq 0.20(?)$
SDSS J005421.42-010921.6	5.09	20.5	1.31	≤ 2.32	≤ 0.68	1.00	≤ 3006
SDSS J013326.84+010637.7*	5.30	20.7	2.71	≤ 2.49	≤ 0.72	1.00	≤ 3425
SDSS J020332.35+001228.6	5.72	20.9	0.27	2.44	0.43	1.00	2028
SDSS J023137.65-072854.5*	5.41	19.5	8.64	≤ 2.66	≤ 0.54	1.00	≤ 2750
SDSS J030331.40-001912.9*	6.08	21.3	1.33	≤ 1.51	≤ 0.82	0.62	≤ 1467
SDSS J033829.31+002156.3	5.00	20.0	6.29	3.93	0.57	1.00	4305
SDSS J035349.72+010404.4	6.07	20.2	0.08	≤ 1.97	≤ 0.49	0.69	≤ 1281
SDSS J073103.12+445949.4	5.01	19.1	3.64	≤ 2.63	≤ 0.13	1.00	≤ 643
SDSS J075618.14+410408.6	5.09	20.1	1.41	3.73	0.69	1.00	4964
SDSS J081827.40+172251.8	6.00	19.3	1.60	3.13	0.16	1.00	971
SDSS J083317.66+272629.0	5.02	20.3	0.04	≤ 2.20	≤ 0.69	1.00	≤ 2901
SDSS J083643.85+005453.3*	5.81	18.8	29.14	≤ 4.19	≤ 0.19	1.00	≤ 1544
SDSS J084035.09+562419.9	5.84	20.0	0.42	2.72	0.67	1.00	3504
SDSS J084119.52+290504.4	5.96	19.6	0.41	≤ 2.10	≤ 0.42	0.69	≤ 1167
SDSS J084229.23+121848.2	6.06	19.9	6.80	≤ 3.66	≤ 0.34	0.61	≤ 1448
SDSS J084627.85+080051.8	5.04	19.6	0.59	≤ 2.44	≤ 0.63	1.00	≤ 2938
BWE 910901+6942	5.47	19.8	0.00	≤ 2.58	≤ 0.60	1.00	≤ 2979
SDSS J090245.77+085115.8	5.22	20.6	1.82	≤ 2.20	≤ 0.66	1.00	≤ 2785
SDSS J091316.56+591921.5	5.11	21.5	0.26	≤ 2.12	≤ 0.76	0.97	≤ 2996
SDSS J091543.64+492416.7	5.20	19.3	0.46	≤ 2.43	≤ 0.55	1.00	≤ 2557
SDSS J092216.82+265359.1	5.06	20.4	0.89	≤ 2.27	≤ 0.71	1.00	≤ 3099
SDSS J092721.82+200123.7	5.77	19.9	1.92	3.51	0.68	1.00	4561
SDSS J095707.67+061059.5	5.19	19.0	4.03	≤ 3.35	≤ 0.33	1.00	≤ 2151
SDSS J101336.33+424026.5	5.06	19.4	1.09	≤ 1.95	≤ 0.71	1.00	≤ 2647
SDSS J103027.10+052455.0	6.31	19.7	0.07	≤ 3.35	≤ 0.63	0.78	≤ 3165
SDSS J104433.04-012502.2	5.78	19.2	4.60	3.64	0.22	1.00	1530
SDSS J104845.05+463718.3	6.23	19.2	2.59	3.23	0.38	1.00	2360
SDSS J111920.64+345248.2	5.02	20.2	2.03	≤ 2.26	≤ 0.53	1.00	≤ 2278
SDSS J113246.50+120901.7	5.17	19.4	9.68	≤ 3.10	≤ 0.21	1.00	≤ 1262
SDSS J113717.73+354956.9	6.01	19.6	0.26	≤ 3.18	≤ 0.58	0.90	≤ 3207
SDSS J114657.79+403708.7*	5.01	19.7	20.25	≤ 2.16	≤ 0.26	1.00	≤ 1072
SDSS J114816.64+525150.3	6.43	19.0	4.23	5.48	0.36	1.00	3801
RD J1148+5253	5.70	23.1	0.00	≤ 2.58	≤ 0.93	0.96	≤ 4406
SDSS J115424.74+134145.8	5.08	20.9	1.76	≤ 2.29	≤ 0.59	1.00	≤ 2571
SDSS J120207.78+323538.8	5.31	18.6	2.93	4.79	0.44	1.00	4046
SDSS J120441.73-002149.6	5.03	19.1	4.33	4.42	0.54	1.00	4547
SDSSp J120823.82+001027.7*	5.27	20.5	0.29	≤ 1.99	≤ 0.91	0.90	≤ 3125
SDSS J122146.42+444528.0	5.19	20.4	6.62	≤ 2.35	≤ 0.37	1.00	≤ 1683
SDSS J124247.91+521306.8*	5.05	20.6	3.97	≤ 1.82	≤ 0.67	1.00	≤ 2344
SDSS J125051.93+313021.9	6.13	19.6	21.44	≤ 4.08	≤ 0.25	1.00	≤ 1954
SDSS J130608.26+035626.3	6.02	19.6	0.04	≤ 2.76	≤ 0.70	0.81	≤ 2992
SDSS J133412.56+122020.7	5.14	19.5	1.05	≤ 2.65	≤ 0.37	1.00	≤ 1869
SDSS J133550.81+353315.8	5.90	19.9	2.12	2.41	0.60	1.00	2762
SDSS J133728.81+415539.9	5.03	19.7	0.33	≤ 2.09	≤ 0.56	1.00	≤ 2261
SDSS J134015.04+392630.8	5.07	19.6	5.46	≤ 2.89	≤ 0.37	1.00	≤ 2031
SDSS J134040.24+281328.2	5.34	19.9	0.09	5.03	0.46	1.00	4404
SDSS J134141.46+461110.3	5.01	21.3	0.01	≤ 2.08	≤ 0.64	1.00	≤ 2558
SDSS J141111.29+121737.4*	5.93	20.0	7.51	≤ 2.21	≤ 0.64	0.68	≤ 1827
SDSS J142325.92+130300.7	5.08	19.6	0.12	≤ 2.47	≤ 0.37	1.00	≤ 1740
FIRST J142738.5+331241	6.12	20.3	2.20	≤ 2.22	≤ 0.69	0.65	≤ 1910
SDSS J143611.74+500706.9	5.83	20.2	0.01	≤ 2.83	≤ 0.72	0.86	≤ 3346
SDSS J144350.67+362315.2	5.29	20.3	40.79	≤ 4.85	≤ 0.00	1.00	$\leq 1.6(?)$
SDSS J151035.29+514841.0	5.11	20.1	0.14	≤ 2.34	≤ 0.44	1.00	≤ 1976
SDSS J152404.10+081639.3	5.08	20.6	0.02	≤ 2.22	≤ 0.75	1.00	≤ 3196
SDSS J160254.18+422822.9	6.07	19.9	2.62	≤ 3.25	≤ 0.32	0.68	≤ 1341
SDSS J161425.13+464028.9	5.31	20.3	7.25	≤ 3.20	≤ 0.28	1.00	≤ 1729
SDSS J162331.81+311200.5	6.25	20.1	1.46	≤ 2.59	≤ 0.43	0.99	≤ 2107
SDSS J162626.50+275132.4	5.30	18.7	7.64	5.35	0.92	1.00	292
SDSS J162629.19+285857.6	5.02	19.9	0.95	≤ 1.32	≤ 0.20	1.00	≤ 503
SDSS J163033.90+401209.6	6.07	20.6	0.49	≤ 1.87	≤ 0.78	0.63	≤ 1752
SDSS J165902.12+270935.1	5.32	18.8	11.12	≤ 3.76	≤ 0.21	1.00	≤ 1547
SDSS J205406.49-000514.8	6.04	20.6	1.47	3.15	0.41	1.00	2501
SDSS J211928.32+102906.6	5.18	20.6	1.49	≤ 1.40	≤ 0.32	1.00	≤ 857
SDSS J222845.14-075755.2*	5.14	20.2	6.81	≤ 1.34	≤ 0.62	1.00	≤ 1593
WFS J2245+0024*	5.17	21.8	2.38	≤ 2.15	≤ 0.89	1.00	≤ 3685
SDSS J231546.57-002358.1	6.12	21.3	1.41	≤ 1.94	≤ 0.76	0.61	≤ 1741

NOTE. — Col. (1): Object name with a * is identified as a hot dust deficient (HDD) quasar; Col. (2): Redshift; Col. (3): Rest-frame 1450Å apparent magnitudes, or $\text{mag}(1450\text{\AA})$; Col. (4): Reduced chi-square, as defined in 2.3; Col. (5): The integrated infrared luminosity ($8\text{--}1000\ \mu\text{m}$) from the fitted two-component SED models; if there are no any detections with $\lambda_{\text{rest}} < 10\ \mu\text{m}$, the derived AGN contribution is put as an upper limit; the host galaxy contribution is treated as an upper limit if there is no detection at $\lambda_{\text{rest}} > 50\ \mu\text{m}$; Col. (6): Relative contribution of the galaxy component to L_{IR} . Col. (7): Correction of the host IR luminosity for the derivation of SFR; Col. (8): Star formation rate estimated from the galaxy component luminosity, assuming the Haro 11 star formation law; a question mark indicates the quasar has a minimal host contribution in the IR, in which case the derived SFR is dubious and not used in the analysis.

TABLE 4
SED DECOMPOSITION RESULTS FOR $z \gtrsim 5.0$ 33 QUASARS (*sample-B*)

Source (1)	z (2)	$m_{1450\text{\AA}}$ (3)	$L_{\text{IR}}(10^{13}L_{\odot})$ (4)	$f_{\text{host,IR}}$ (5)	SFR(M_{\odot}/yr) (6)
SDSS J003311.40-012524.9	6.13	21.53	0.81	0.69	1079
CFHQS J005006+344522	6.25	19.84	≤ 2.99	≤ 0.46	≤ 2643
CFHQS J005502+014618	6.02	21.82	0.28	0.33	179
CFHQS J010250-021809	5.95	22.02	≤ 1.27	≤ 0.88	≤ 2141
SDSS J012958.51-003539.7	5.78	22.28	1.16	0.90	2013
CFHQS J013603+022605	6.21	22.04	≤ 3.09	≤ 0.65	≤ 3852
CFHQS J021013-045620	6.44	22.25	0.19	0.25	92
CFHQS J021627-045534	6.01	24.15	≤ 1.11	≤ 0.98	≤ 2082
CFHQS J022122-080251	6.16	21.98	≤ 2.26	≤ 0.93	≤ 4016
CFHQS J022743-060530	6.20	21.41	≤ 1.08	≤ 0.73	≤ 1522
SDSS J023930.24-004505.4	5.82	22.28	≤ 1.66	≤ 0.93	≤ 2945
RD J0301+0020	5.50	23.40	0.52	0.91	906
CFHQS J031649-134032	5.99	21.72	≤ 3.89	≤ 0.95	≤ 7077
TN J0924-2201	5.20	—	≤ 1.04	≤ 0.84	≤ 1659.35
CFHQS J105928-090620	5.92	20.75	≤ 2.06	≤ 0.60	≤ 2377
ULAS J1120+0641	7.08	—	0.42	0.63	513
ULAS J131911.29+095051.4	6.13	19.65	3.47	0.59	3927
SDSS J142516.30+325409.0	5.85	20.62	≤ 1.89	≤ 0.50	≤ 1810
CFHQS J142952+544717	6.21	20.59	2.68	0.63	3246
SDSS J150941.78-174926.8	6.12	19.63	≤ 2.52	≤ 0.43	≤ 2057
SDSS J162100.70+515544.8	5.71	19.89	≤ 4.21	≤ 0.18	≤ 1438
SDSS J164121.64+375520.5	6.04	21.19	≤ 1.17	≤ 0.71	≤ 1603
SDSS J205321.77+004706.8	5.92	21.20	≤ 1.34	≤ 0.76	≤ 1946
CFHQS J210054-171522	6.09	21.37	≤ 3.46	≤ 0.24	≤ 1604
SDSS J214755.40+010755.0	5.81	21.65	≤ 1.44	≤ 0.65	≤ 1782
CFHQS J222901+145709	6.15	21.90	0.19	0.06	22
CFHQS J224237+033421	5.88	22.09	≤ 1.48	≤ 0.90	≤ 2561
SDSS J230735.35+003149.4	5.87	21.73	≤ 1.68	≤ 0.45	≤ 1460
SDSS J231038.88+185519.7	6.00	19.30	6.07	0.69	7996
CFHQS J231802-024634	6.05	21.55	≤ 1.38	≤ 0.82	≤ 2178
SDSS J232908.28-030158.8	6.43	21.53	≤ 1.38	≤ 0.00	$\leq 0.0(?)$
CFHQS J232914-040324	5.90	21.96	≤ 1.14	≤ 0.86	≤ 1886
SDSS J235651.58+002333.3	6.00	21.77	≤ 1.06	≤ 0.81	≤ 1653

NOTE. — Col. (1): Quasar name; Col. (2): Redshift; Col. (3): Rest-frame 1450Å AB apparent magnitudes, or $\text{mag}(1450\text{\AA})$; Col. (4): The integrated infrared luminosity (8-1000 μm) from the fit two-component SED models; if there is no detection with $\lambda_{\text{rest}} < 10\mu\text{m}$, the derived AGN contribution is put as an upper limit; the host contribution is treated as an upper limit if the quasar is not detected at $\lambda_{\text{rest}} > 50\mu\text{m}$; Col. (5): Relative contribution of the galaxy component to L_{IR} ; Col. (6): Star formation rate estimated from the galaxy component luminosity, assuming the Haro 11 star formation law; a question mark indicates the quasar has a minimal host contribution in the IR, in which case the derived SFR is dubious and not used in the analysis.

TABLE 5
SED DECOMPOSITION RESULTS FOR THE STACKED QUASAR SEDS

Source (1)	N (2)	Redshift (3)	$L_{\text{IR}}/10^{13}L_{\odot}$ (4)	$f_{\text{host,IR}}$ (5)	χ^2_{ν} (6)	SFR(M_{\odot}/yr) (7)
FIR-detected	10	5.34	4.08	0.47	0.63	3666
partly-detected	14	5.31	2.04	0.00	0.20	$\lesssim 1.5(?)$
non-detected	33	5.20	0.87	0.00	0.61	$\sim 0(?)$

NOTE. — Results of full IR fits. Upper-limit data points are included in the evaluation process.

Col. (1): Type of stacked SED; Col. (2): The number of stacked quasars; Col. (3): Average redshift; Col. (4): The total infrared luminosity (8-1000 μm) estimated from the “Haro 11 + AGN” two-component SED fit; Col. (5): The fraction of luminosity of host template contribution to the whole fit SED, based on result from the “Haro 11 + AGN” decomposition; Col. (6): Reduced chi-square from the “Haro 11 + AGN” decomposition; Col. (7): Estimation of the star formation rate.

The narrow-line regions (NLRs) of quasars at $z \sim 1 - 4$ are also found to be around solar-metallicity without strong evolution (Matsuoka et al. 2009). In contrast with the BLRs, the typical size of the NLRs ($\sim 10^{1-4}$ pc, Bennert et al. 2006b,a) is comparable to the size of the host galaxies. The only quasar beyond $z \gtrsim 5$ with a NLR metallicity constraint is TN J0924–2201, a type-2 radio galaxy at $z = 5.19$ (Matsuoka et al. 2011). Considering the small sample size and uncertainty of the metallicity calibration, the result for TN J0924–2201 does not provide much knowledge of the metallicity in the $z \gtrsim 5$ quasars. We do not have observational constraints on the metallicity of these quasar hosts from emission line analysis.

Another possible approach to get metallicity constraints on (or near) distant quasar hosts is from analyzing the absorbers with high H I content ($N_{\text{H I}} \gtrsim 10^{20} \text{cm}^{-2}$), or so-called damped Lyman-alpha (DLA) systems, at the redshift of the quasar (Hennawi et al. 2009; Zafar et al. 2011). Hennawi et al. (2009) reported the discovery of a bright Lyman- α blob associated with the $z = 3$ quasar SDSS J124020.91+145535.6 and gave a lower limit to the gas metallicity $Z \gtrsim 1/10 Z_{\odot}$. Zafar et al. (2011) studied a physical quasar pair Q0151+048 ($z \sim 1.9$) and suggested an overall metallicity of $0.01 Z_{\odot}$ for a DLA associated with one member. The redshifts of these two quasars are relatively low. It is also not clear if they are representative of the general population. As argued by Finley et al. (2013), statistical study shows the absorption of the associated DLAs is more likely to happen in the galaxies neighboring the quasar, rather than in the AGN host galaxy. Further detailed studies on larger samples are needed to make any conclusive argument.

Several works argued that some massive galaxies at high- z have solar metallicity (e.g., Maiolino et al. 2008; Mannucci et al. 2009; Rawle et al. 2014). It is possible that these objects are mature and highly evolved. However, we should be cautious about the derived metallicity with very limited data points for individual sources. Convincing measurements of metallicity at high- z require more understanding of the ISM in these systems. For $2.0 < z < 2.5$ galaxies, statistical studies based on multiple metallicity tracers show that their metallicities drop at large masses (Maier et al. 2014; Cullen et al. 2014). For the very early Universe, simulations suggest population III stars contribute little to the chemical enrichment of the ISM (Valiante et al. 2009). The existence of a huge population of low-metallicity systems between the cosmic reionization and $z > 2.5$ should be expected. Since high- z quasars are originally identified by their AGN features, the properties of their host galaxies should not be much biased by the selection. It is therefore plausible that the high- z quasar host galaxies have metallicities moderately, if not substantially, below solar.

In this work, hints for the low-metallicity of the AGN host galaxies at $z \gtrsim 5$ are from the successful reproduction of the observed SEDs based on two-component fits, as shown in Section 3.3. The high dust temperature and boosted mid-IR emission are two major features of the IR SED of Haro 11, a dwarf galaxy with metallicity $Z \sim 1/3 Z_{\odot}$. For the IR SED of these quasars, the low-metallicity Haro 11 template works significantly better

than the normal SF templates.

Xu et al. (2015b) discovered a warm mid-IR component of some type-1 quasars at $z \sim 0.7 - 2.5$, which can not be reproduced by the combination of the AGN template and normal SF template. This warm excess is found to be more prominent at higher redshifts in their sample. As shown in Section 3.3, a strong mid-IR SED excess also does exist when fitting the host galaxy with normal SF templates for the $z \gtrsim 5$ quasars. In contrast, by introducing the Haro 11 template, the mid-IR part of the SED of the $z \gtrsim 5.0$ quasars is reproduced better: there is no strong hint of the warm excess for the majority of the quasars. The low-metallicity of the host galaxy is a possible explanation for many such warm excesses at high- z : the dust population in the low-metallicity environment tends to be dominated by small-size grains, which would result in substantial emission in the mid-infrared. Due to the increase of the mid-IR emission, the effective dust temperature fit from the whole infrared SED is also boosted. Nonetheless, a small number of $z \gtrsim 5$ quasars still show a mid-IR warm excess, such as J0338+0021 and J1602+4228, even with the Haro 11 template fitting. We suggest that such additional warm excess not reproduced by the “Haro 11 + AGN” SED model could be due to an extreme circumnuclear starburst or that the host galaxy has a much lower metallicity.

5.3. The Star Formation Rates of Quasars at $z \gtrsim 5$

In estimating a SFR, the largest uncertainty comes from the assumed star formation calibration. In Appendix B, the star formation determination for the low-metallicity dwarf galaxies is discussed. We show that the Kennicutt (1998) IR star formation law is still valid to roughly estimate the obscured star formation rates for the low-metallicity dwarf galaxies, including Haro 11. Besides the obscured star formation, we also consider the unobscured star formation as revealed by the UV emission. As shown in Appendix B.2, Haro 11 has a low UV star formation rate estimate, which is only $\sim 10\%$ of that deduced from the far-IR. For a $2000 M_{\odot}/\text{yr}$ infrared SFR, the corresponding UV SFR would be $200 M_{\odot}/\text{yr}$, consistent with the upper limit given for the archetypal $z \sim 6$ quasar J1148+5251 (Mechtley et al. 2012). The UV star formation of high-luminosity quasar host galaxies at $z \sim 2.6$ is also found to be quite weak (Cai et al. 2014). These examples indicate that a low contribution to the estimated SFR from the UV is appropriate for quasar host galaxies identical to those for J1148+5251 and the Cai et al. (2014) quasar sample. However, we can not rule out the possibility that some of the host galaxies at the epoch of reionization have larger escape fractions than Haro 11 and hence a large fraction of UV emission, causing us to underestimate their total SFRs.

Many censored data points also make the SFR estimation difficult. For the quasars with at least two detections in the far-IR, the host galaxies are reasonably well fit. The derived star formation rates are on the order of $10^3 M_{\odot}/\text{yr}$, a typical value also found by other authors (e.g., Wang et al. 2008b; Leipski et al. 2014). For quasars without any far-IR detections, we could only determine the upper-limits of their SFRs. As described in Section 2.3, we consider all the censored data points during the fitting process. For sources without far-IR detections, the fitted upper limits on the SFRs are based

on templates constrained by multiple 3σ non-detections and result in overestimated SFR constraints. To solve this problem, we scale the host template to each non-detected 3σ -limit observation, derive the respective SFR, and pick the lowest one as the final constraint on the quasar host SFR. During this process, the contribution of the fitted AGN component is fixed and subtracted when deriving the SFR.

For the HDD quasars, the AGN template fails at $\lambda \gtrsim 1.0\mu\text{m}$. In addition, none of them are detected in the far-IR. To derive conservative upper limits for their SFRs, we assume that all their far-IR emission comes from the host galaxy. Consequently, we ignore the fitted AGN component when we scale the host template to the observations.

We ignore the results for J0017–1000 and J1443+3623 of *sample-A*, whose host contribution is too minimal to be evaluated. From Kaplan-Meier analysis⁵, the mean infrared host galaxy luminosity of the *sample-A* is

$$\langle \log(L_{\text{SF,IR}}/L_{\odot}) \rangle = 12.51 \pm 0.10, \quad (\text{sample A})$$

which corresponds to an average star formation rate

$$\langle \text{SFR} \rangle = 621^{+161}_{-128} M_{\odot}/\text{yr}. \quad (\text{sample A})$$

Another approach to compute the average star formation rate is to analyze the stacked SEDs. As shown in Figure 4 and Table 5, the fraction of the host contribution is too small to give any physical constraints on the SFR of the stacked SEDs of *Herschel* partly- and non-detected quasars. We simply conclude substantial star formation only happens in the *Herschel* FIR-detected stacked SED, whereas the star formation in other stacked SEDs is minimal and set to be zero. Then an arithmetic mean of *sample-A* is

$$\langle \text{SFR} \rangle = 643 M_{\odot}/\text{yr}. \quad (\text{A-stacked})$$

This result is almost the same as that from the Kaplan-Meier analysis for individual sources, confirming the validity of the result from the Kaplan-Meier estimator.

For *sample-B*, after rejecting SDSS J2329-0301 due to its minimal host contribution, we use the Kaplan-Meier approach to derive a mean infrared luminosity for 32 quasars

$$\langle \log(L_{\text{SF,IR}}/L_{\odot}) \rangle = 12.27 \pm 0.22, \quad (\text{sample B})$$

which corresponds to an average star formation rate

$$\langle \text{SFR} \rangle = 357^{+236}_{-142} M_{\odot}/\text{yr}. \quad (\text{sample B})$$

This estimate is subject to systematic errors because the majority of the *sample-B* members only have submillimeter measurements at 1.2 mm, and these fall well beyond the peaks of their far-IR SEDs. Therefore, any deviation of the SED from the template will result in significant errors in the estimate of infrared luminosity. Nonetheless, within the errors, this $\langle \text{SFR} \rangle$ is similar to that from *sample-A*. In fact, we will show in Section 5.5 that the indicated slightly lower SFRs for *sample-B* is as might be expected from the generally lower luminosities of their AGNs.

⁵ As implemented in the Astronomy Survival Analysis Package (ASURV, Lavalley et al. 1992)

We believe that the average SFR estimated above is robust even if Haro 11 is not representative for some quasar host galaxies. As shown in Section 3.1, the results from the Haro 11 template are not substantially different from the normal SF templates in Rieke et al. (2009). In fact, the AGN template is principally fixed by data points at $\sim 1 - 5\mu\text{m}$, leaving the SF template to be matched to the mid-IR to far-IR SED. The large range between the maximum star formation rates and the averages suggests that star formation is very “bursty” in the host galaxies, and that the averages can be considered to represent the rates integrated over time. These issues are discussed in Section 5.5.

5.4. AGN Luminosity

The total AGN luminosity can be estimated from integrating the Elvis template (e.g., Hao et al. 2014, Xu et al. 2015b). Since our fits are limited to the infrared ($1\text{--}1000\mu\text{m}$), the total AGN luminosity can be derived by scaling an infrared-to-bolometric correction of 5.28 (Xu et al. 2015b) to the AGN total infrared luminosity $L_{\text{IR,AGN}}$ ⁶. Before that, we check the validity of the Elvis template in the UV/optical bands. As shown in Figure 4, the Elvis et al. (1994) template reproduces the UV to mid-IR stacked SED of these quasars well. For individual sources, although there are some detailed offsets, the Elvis template generally matches the observations. The monochromatic flux at rest frame 1450\AA is a frequently used indicator of AGN UV continuum brightness in the literature. By applying a scaling factor of 4.65^7 on the $\nu L_{\nu}(1450\text{\AA})$, the AGN bolometric luminosity can be estimated. Taking $\text{mag}(1450\text{\AA})$ in the literature as a crude but independent tracer of AGN bolometric luminosity, in Figure 7, we plot the $\text{mag}(1450\text{\AA})$ -based AGN bolometric luminosities against the L_{FIR} -based ones. There is a small offset from 1:1 on the correlation between the AGN luminosities from $\text{mag}(1450\text{\AA})$ and from the infrared bolometric correction, which can be explained by possible UV extinction. In summary, though the normalization of the AGN template is constrained by the rest-frame near-IR to mid-IR data points, the residuals of observed UV/optical SEDs from the IR fit to the Elvis template are generally small.

Leipski et al. (2014) pointed out 11 quasars with a dearth of very hot dust. We confirm their peculiarity by comparing their observed SEDs with the Elvis template. If normalized at UV/optical wavelengths, the Elvis template clearly overestimates the observed SED beyond rest frame $1\mu\text{m}$. Since we do not have a clear picture of the full wavelength SED of these HDD objects, their luminosities are hard to derive. We still rely on the L_{FIR} -based luminosity, rather than UV-based luminosity, for two reasons: (1) the UV-optical SED could suffer extinction, thus underestimating the total bolometric luminosity; (2) the UV emission is not isotropic while the sources are optically thin in the near- and mid-IR (Marconi et al. 2004). Judging by the UV/optical observation, we do not

⁶ For quasars with L_{IR} upper limits in Table 3, we can still get their AGN total infrared luminosities: $L_{\text{IR,AGN}} = L_{\text{IR}}(1 - f_{\text{host,IR}})$, where $f_{\text{host,IR}}$ is the host galaxy contribution upper limit.

⁷ This value is derived based on the Richards et al. (2006) template.

expect the template-derived luminosity has more than one order of magnitude deviation from the observed one. In Figure 7, it is interesting to note the HDD quasars in this work generally follow the same trend as normal quasars.

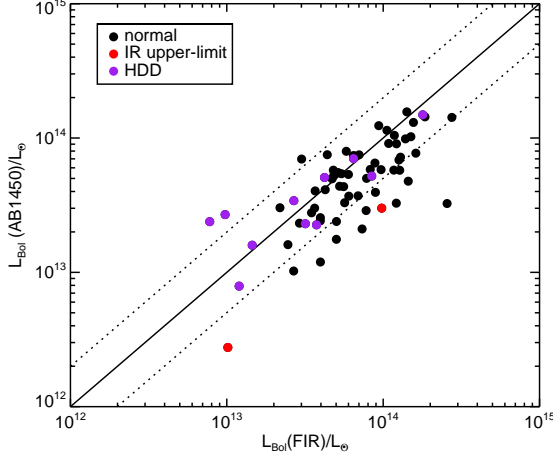


FIG. 7.— Comparison of AGN luminosities derived from $\text{mag}(1450\text{\AA})$ and infrared SED fits. 0.3 dex offsets are shown as dotted lines. Purple dots are for the 11 HDD quasars, red dots for two quasars with upper-limit of $L_{\text{AGN,IR}}$, black dots for other quasars.

Finally, we can derive the average AGN bolometric luminosity of *sample-A* with standard error to be:

$$\langle L_{\text{AGN}} \rangle = 5.287 \times \langle L_{\text{AGN,IR}} \rangle \approx (7.48 \pm 0.62) \times 10^{13} L_{\odot} \quad (\text{sample A})$$

Similarly, *sample-B* has

$$\langle L_{\text{AGN}} \rangle \approx (2.63 \pm 0.14) \times 10^{13} L_{\odot} \quad (\text{sample B})$$

This value is $\sim 36\%$ of *sample-A*

5.5. Implications for BH-galaxy Evolution

We now compare the relative strength between SF activities and AGN luminosities of $z \gtrsim 5$ quasars with that of relatively low- z and intermediate- z quasars. In Figure 8, we put the average values for $z \gtrsim 5$ quasars on the relation between SF IR luminosity, $L_{\text{SF,IR}}$, and AGN luminosity, L_{AGN} , for the Xu et al. (2015b) type-1 quasar sample. The average properties of the $z \gtrsim 5$ quasars fall along the fit relation. This is unexpected, however, since quasars at $z \gtrsim 5$ and those at $z < 3$ should be in different star formation phases. From a theoretical perspective, there should be no star formation main sequence as is the case in the $z < 3$ Universe, but bursts of star formation and periods of near-zero star formation rates, likely due to the dynamically disturbed gas within the galaxy halo (e.g., Muratov et al. 2015). Current observations suggest the star formation in some $z > 5$ quasars is extremely vigorous with SFRs at levels of $\gtrsim 10^3 M_{\odot}/\text{yr}$ (e.g., Wang et al. 2008b) or relatively mild with SFRs $\lesssim 50 M_{\odot}/\text{yr}$ (e.g., Willott et al. 2013). Despite this large dispersion, an underlying relation between the average host star formation and AGN luminosity, which has been suggested for very luminous AGNs

at $z \lesssim 2.5$ (e.g., Netzer 2009; Rosario et al. 2012), seems to already exist at $z \sim 5 - 6$.

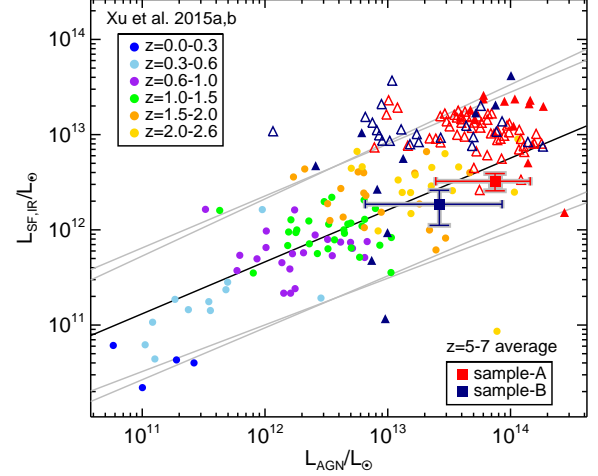


FIG. 8.— The IR luminosity of the star-formation component $L_{\text{SF,IR}}$ versus the total AGN luminosity L_{AGN} for quasars at different redshifts. Only type-1 AGNs in Xu et al. (2015b) are plotted (small dots). The solid black line is the best-fit unweighted relationship for all type-1 AGN in Xu et al. (2015b) with a slope of 0.55, with shifted relation by $1-\sigma$ error of either slope or intercept shown as grey solid lines. Our measurements for individual $z \gtrsim 5$ quasars are also shown as red (*sample-A*) and blue (*sample-B*) triangles, with filled for detections and open for upper-limits. We also plot the Kaplan-Meier mean of $z \gtrsim 5$ AGN host galaxy IR luminosities at mean AGN luminosities for *sample-A* (red square) and *sample-B* (blue square), with horizontal error bars showing the range including 80% of the sample's sources.

By taking an average of the star formation rates of quasar host galaxies in the largest sample at $z \sim 5 - 7$, we can retrieve a rough time-averaged star formation rate during the lifetime of these quasar host galaxies. In other words, we assume that the relative number of host galaxies with very active star formation ($\text{SFR} \sim 10^3 M_{\odot}/\text{yr}$) to those without significant star formation ($\text{SFR} \lesssim 10 M_{\odot}/\text{yr}$) reflects the relative time duration of the star-bursting phase to the quiescent phase of the galaxies. Since stars lose mass quickly after leaving the main sequence, we can ignore their contribution to the stellar mass of the galaxy. The main sequence lifetime of a star with mass M is

$$\tau_{\text{MS}} = 10 \times (M/M_{\odot})^{-2.5} \text{ Gyr} \quad (7)$$

Then we have a simple model relating the stellar mass M_* to the galaxy growth time Δt and the initial mass function $\xi(m)$ as:

$$\langle M_* \rangle \sim \int_0^{\Delta t} \int_{M_{\text{low}}}^{M_{\odot}(t/10)^{-0.4}} \xi(m) \langle \text{SFR} \rangle dm dt, \quad (8)$$

where M_{low} is the minimum stellar mass, which is assumed to be $0.1 M_{\odot}$; $M_{\odot}(t/10)^{-0.4}$ is the maximum stellar mass of stars that are still on the main sequence at time t (unit: Gyr); Δt is the epoch of galaxy mass assembly.

To start, we simply assume a standard Salpeter IMF (Salpeter 1955), and estimate the increase in host galaxy stellar mass since the start of the cosmic reionization,

TABLE 6
ESTIMATION OF A TYPICAL HOST GALAXY MASS

IMF	SFR (M_{\odot}/yr) ^a	M_* (M_{\odot}) ^b $z_0 = 8.8$	M_* (M_{\odot}) ^b $z_0 = 20$
Salpeter	621	3.02×10^{11}	5.42×10^{11}
Kroupa	534 ^c	3.00×10^{11}	4.80×10^{11}

NOTE. — ^a Values derived from *sample-A*; ^b Stellar masses derived based on Equation 8, z_0 is the redshift when the first galaxies begin to assemble their masses; ^c Kennicutt & Evans (2012) updated their original IR star formation calibration (Kennicutt 1998) with the Kroupa & Weidner (2003) IMF. The SFR should be reduced to $\sim 86\%$.

i.e., $z = 8.8_{-1.4}^{+1.7}$ (Planck Collaboration et al. 2015), corresponding to a Universe age $0.573_{+0.150}^{-0.122}$ Gyr. Then the time duration Δt from reionization to the average age of the quasars in our sample ($\langle z \rangle = 5.5$) is $\Delta t = 0.489_{-0.150}^{+0.122}$ Gyr. Taking the average star formation rate for *sample-A* and solving the integration in Equation 8, we derive the stellar mass that could form in a $z \sim 5.5$ quasar to be

$$\langle M_* \rangle \approx 3.0_{-0.9}^{+0.7} \times 10^{11} M_{\odot}. \quad (9)$$

This rough estimate is not highly sensitive to the starting redshift, nor to the form of the standard IMF (see Table 6). For example, if we assume a start at $z = 20$, the total stellar mass increases by less than a factor of two. We can also change the power-law Salpeter IMF to a more realistic Kroupa & Weidner (2003) IMF with a turnover below $\sim 1 M_{\odot}$ and use the updated IR star formation calibration in Kennicutt & Evans (2012). The derived M_* is lower by up to 10%. As a result, we estimate that the SFRs we deduce for the host galaxies are likely to result in formation of a net mass $(3 - 5) \times 10^{11} M_{\odot}$ during the major assembly phases for these quasar host galaxies. Although this result was derived for *sample-A*, the high average SFR also exhibited for *sample-B* indicates it is generally true for high-redshift quasars.

We compare this mass with typical masses for the central black holes in these galaxies, $\sim 10^8 - 10^9 M_{\odot}$ (e.g., Jiang et al. 2007; Kurk et al. 2007, 2009; Willott et al. 2010a; De Rosa et al. 2011; Jun et al. 2015). It appears that the formation of stellar mass is adequate to establish $M_{\text{BH}}/M_{*,\text{total}}$ at 0.1 - 1%, which is in good agreement with estimates of this parameter locally (e.g., Kormendy & Ho 2013 and references therein), and with the evidence at $z \lesssim 2$ that the ratio does not evolve substantially with redshift. If some of the $z \gtrsim 5$ host galaxies have a larger escape fraction than Haro 11 and hence their SFRs are under-represented by our approach, this conclusion is strengthened. Our conclusion agrees with the measurement of the dynamical masses of these systems (Willott et al. 2015) that also indicates very little evolution of this ratio with redshift up to $z \sim 6$.

6. SUMMARY

In this work, we describe an effective strategy to analyze the infrared output of high- z quasars. A two-component SED model to quantify and distinguish star formation and nuclear activity is proposed: the host galaxy component can be represented by the SED of

Haro 11, a low-metallicity dwarf galaxy with extreme compact star-forming regions; the AGN component can be represented by the Elvis et al. (1994) AGN template with the IR star formation contribution subtracted. Such a simple model can help us have a better idea of the AGN and star formation contribution for these high- z objects when only limited observations are available. Using this method, we have analyzed the AGN contribution and host galaxy contribution to the infrared SEDs of 69 quasars with *Herschel* observations in Leipski et al. (2014) and another 33 quasars in the literature. Our major conclusions are as follows:

1. Haro 11 is a faithful representation for the host galaxies of $z \gtrsim 5$ quasars. Besides its moderately low-metallicity, Haro 11 has a very high star formation surface density, which is common for high-redshift galaxies as well as quasar hosts.

2. The AGN contribution to the UV-to-IR SEDs of $z \gtrsim 5$ quasars can be well-represented by the Elvis et al. (1994) AGN template with the star formation contribution to the IR subtracted. For the infrared, except for the HDD quasars, there is no detectable over-prediction of the observed flux from the modified AGN template. After subtracting the AGN contribution in the IR, the residual flux can be interpreted as the IR contribution from host galaxy star formation, which is well-fit by the Haro 11 template.

3. The warm excess found for some high- z quasars (see, e.g., Xu et al. 2015b) can be produced by the introduction of the Haro 11 template, suggesting this feature may reflect the low-metallicity of the quasar host. The Haro 11 template also shares the high dust temperature found in the far-IR measurements of high- z quasars. That is, these two features can be explained by the dust properties and distribution in the low-metallicity environment.

4. The average SFR of the $z \sim 5 - 6.5$ quasars observed by *Herschel* is $\sim 620 M_{\odot}/\text{yr}$, considering both far-IR detected and non-detected observations.

5. For the overall population of $z \gtrsim 5$ quasars, the total AGN luminosity $\langle L_{\text{AGN}} \rangle$ and average infrared luminosity from star formation $\langle L_{\text{SF,IR}} \rangle$ fall along the relation defined by $z < 2.6$ quasars. This is unexpected since the star formation at $z \gtrsim 5$ and that at $z \lesssim 3$ should experience different phases (e.g., bursty vs. relatively steady).

6. Assuming the sample averaged SFR is a rough time-averaged SFR estimate during the lifetime of the quasar host galaxies, we found the $z \sim 5 - 6$ quasar host galaxies could form $\sim (3 - 5) \times 10^{11} M_{\odot}$ of stars. With the black hole mass measurements of these quasars, such massive host galaxies make possible a local BH-galaxy mass relation $M_{\text{BH}}/M_* \sim 0.1 - 1\%$ at $z \sim 6$, suggesting there may not be strong redshift evolution of the BH-galaxy mass ratio.

We are grateful to the referee for comments and suggestions that improved the clarity of this paper. We thank Eiichi Egami, Richard Green, Daniel Stark and Xiaohui Fan for helpful suggestions. This work was supported by NASA grants NNX13AD82G and 1255094. This publication has made use of data products from the *Wide-field Infrared Survey Explorer*, which is a joint project of the University of California, Los Angeles, and the Jet

Propulsion Laboratory/California Institute of Technology, funded by the National Aeronautics and Space Administration. This research has also benefited from the

use of the NASA/IPAC Extragalactic Database (NED) which is operated by the Jet Propulsion Laboratory, California Institute of Technology, under contract with the National Aeronautics and Space Administration.

REFERENCES

- Adamo, A., Östlin, G., Zackrisson, E., et al. 2010, *MNRAS*, 407, 870
- Bañados, E., Venemans, B. P., Morganson, E., et al. 2014, *AJ*, 148, 14
- Barnett, R., Warren, S. J., Banerji, M., et al. 2015, *A&A*, 575, A31
- Beelen, A., Cox, P., Benford, D. J., et al. 2006, *ApJ*, 642, 694
- Bennert, N., Jungwiert, B., Komossa, S., Haas, M., & Chini, R. 2006a, *A&A*, 459, 55
- . 2006b, *A&A*, 456, 953
- Bergvall, N., & Östlin, G. 2002, *A&A*, 390, 891
- Bergvall, N., Zackrisson, E., Andersson, B.-G., et al. 2006, *A&A*, 448, 513
- Bertoldi, F., & Cox, P. 2002, *A&A*, 384, L11
- Blain, A. W., Barnard, V. E., & Chapman, S. C. 2003, *MNRAS*, 338, 733
- Cai, Z., Fan, X., Noterdaeme, P., et al. 2014, *ApJ*, 793, 139
- Calura, F., Gilli, R., Vignali, C., et al. 2014, *MNRAS*, 438, 2765
- Calzetti, D. 2001, *PASP*, 113, 1449
- Carilli, C. L., & Walter, F. 2013, *ARA&A*, 51, 105
- Casey, C. M. 2012, *MNRAS*, 425, 3094
- Cox, P., Krips, M., Neri, R., et al. 2011, *ApJ*, 740, 63
- Cullen, F., Cirasuolo, M., McLure, R. J., Dunlop, J. S., & Bowler, R. A. A. 2014, *MNRAS*, 440, 2300
- da Cunha, E., Groves, B., Walter, F., et al. 2013, *ApJ*, 766, 13
- Daddi, E., Dickinson, M., Chary, R., et al. 2005, *ApJ*, 631, L13
- Daddi, E., Dickinson, M., Morrison, G., et al. 2007, *ApJ*, 670, 156
- De Rosa, G., Decarli, R., Walter, F., et al. 2011, *ApJ*, 739, 56
- Dunne, L., & Eales, S. A. 2001, *MNRAS*, 327, 697
- Dwek, E., Staguhn, J. G., Arendt, R. G., et al. 2011, *ApJ*, 738, 36
- Elvis, M., Wilkes, B. J., McDowell, J. C., et al. 1994, *ApJS*, 95, 1
- Elvis, M., Hao, H., Civano, F., et al. 2012, *ApJ*, 759, 6
- Engelbracht, C. W., Gordon, K. D., Rieke, G. H., et al. 2005, *ApJ*, 628, L29
- Engelbracht, C. W., Rieke, G. H., Gordon, K. D., et al. 2008, *ApJ*, 678, 804
- Fan, X., Hennawi, J. F., Richards, G. T., et al. 2004, *AJ*, 128, 515
- Fan, X., Strauss, M. A., Becker, R. H., et al. 2006, *AJ*, 132, 117
- Finley, H., Petitjean, P., Pâris, I., et al. 2013, *A&A*, 558, A111
- Fisher, D. B., Bolatto, A. D., Herrera-Camus, R., et al. 2014, *Nature*, 505, 186
- Fritz, J., Franceschini, A., & Hatziminaoglou, E. 2006, *MNRAS*, 366, 767
- Galametz, M., Madden, S., Galliano, F., et al. 2009, *A&A*, 508, 645
- Galametz, M., Kennicutt, R. C., Albrecht, M., et al. 2012, *MNRAS*, 425, 763
- Galliano, F., Madden, S. C., Jones, A. P., Wilson, C. D., & Bernard, J.-P. 2005, *A&A*, 434, 867
- Galliano, F., Madden, S. C., Jones, A. P., et al. 2003, *A&A*, 407, 159
- Greve, T. R., Vieira, J. D., Weiß, A., et al. 2012, *ApJ*, 756, 101
- Grimes, J. P., Heckman, T., Strickland, D., et al. 2007, *ApJ*, 668, 891
- Groves, B., Dopita, M. A., Sutherland, R. S., et al. 2008, *ApJS*, 176, 438
- Haas, M., Klaas, U., Müller, S. A. H., et al. 2003, *A&A*, 402, 87
- Hanish, D. J., Teplitz, H. I., Capak, P., et al. 2013, *ApJ*, 768, 13
- Hao, H., Elvis, M., Civano, F., & Lawrence, A. 2011, *ApJ*, 733, 108
- Hao, H., Elvis, M., Civano, F., et al. 2010, *ApJ*, 724, L59
- . 2014, *MNRAS*, 438, 1288
- Hayes, M., Östlin, G., Atek, H., et al. 2007, *MNRAS*, 382, 1465
- Heckman, T. M., & Best, P. N. 2014, *ARA&A*, 52, 589
- Hennawi, J. F., Prochaska, J. X., Kollmeier, J., & Zheng, Z. 2009, *ApJ*, 693, L49
- Hodge, J. A., Riechers, D., Decarli, R., et al. 2015, *ApJ*, 798, L18
- Hönig, S. F., & Kishimoto, M. 2010, *A&A*, 523, A27
- Hopkins, A. M., Schulte-Ladbeck, R. E., & Drozdovsky, I. O. 2002, *AJ*, 124, 862
- Huang, J.-S., Rigopoulou, D., Magdis, G., et al. 2014, *ApJ*, 784, 52
- Isobe, T., Feigelson, E. D., & Nelson, P. I. 1986, *ApJ*, 306, 490
- Jahnke, K., Bongiorno, A., Brusa, M., et al. 2009, *ApJ*, 706, L215
- James, B. L., Tsamis, Y. G., Walsh, J. R., Barlow, M. J., & Westmoquette, M. S. 2013, *MNRAS*, 430, 2097
- Jiang, L., Fan, X., Vestergaard, M., et al. 2007, *AJ*, 134, 1150
- Jiang, L., Fan, X., Hines, D. C., et al. 2006, *AJ*, 132, 2127
- Jiang, L., Fan, X., Annis, J., et al. 2008, *AJ*, 135, 1057
- Jiang, L., Fan, X., Brandt, W. N., et al. 2010, *Nature*, 464, 380
- Jiang, L., Egami, E., Fan, X., et al. 2013, *ApJ*, 773, 153
- Juarez, Y., Maiolino, R., Mujica, R., et al. 2009, *A&A*, 494, L25
- Jun, H. D., Im, M., Lee, H. M., et al. 2015, *ApJ*, 806, 109
- Kennicutt, R. C., & Evans, N. J. 2012, *ARA&A*, 50, 531
- Kennicutt, Jr., R. C. 1998, *ARA&A*, 36, 189
- Kennicutt, Jr., R. C., Tamblyn, P., & Congdon, C. E. 1994, *ApJ*, 435, 22
- Kirkpatrick, A., Pope, A., Alexander, D. M., et al. 2012, *ApJ*, 759, 139
- Kormendy, J., & Ho, L. C. 2013, *ARA&A*, 51, 511
- Kroupa, P., & Weidner, C. 2003, *ApJ*, 598, 1076
- Kurk, J. D., Walter, F., Fan, X., et al. 2009, *ApJ*, 702, 833
- . 2007, *ApJ*, 669, 32
- Lavalley, M., Isobe, T., & Feigelson, E. 1992, in *Astronomical Society of the Pacific Conference Series*, Vol. 25, *Astronomical Data Analysis Software and Systems I*, ed. D. M. Worrall, C. Biemesderfer, & J. Barnes, 245
- Le Floc'h, E., Pérez-González, P. G., Rieke, G. H., et al. 2004, *ApJS*, 154, 170
- Lebouteiller, V., Barry, D. J., Spoon, H. W. W., et al. 2011, *ApJS*, 196, 8
- Lee, J. C., Gil de Paz, A., Tremonti, C., et al. 2009, *ApJ*, 706, 599
- Leipski, C., Meisenheimer, K., Walter, F., et al. 2013, *ApJ*, 772, 103
- . 2014, *ApJ*, 785, 154
- Leitet, E., Bergvall, N., Piskunov, N., & Andersson, B.-G. 2011, *A&A*, 532, A107
- Li, Y., Hopkins, P. F., Hernquist, L., et al. 2008, *ApJ*, 678, 41
- Lutz, D. 2014, *ARA&A*, 52, 373
- Madau, P., & Dickinson, M. 2014, *ARA&A*, 52, 415
- Madden, S. C., Galliano, F., Jones, A. P., & Sauvage, M. 2006, *A&A*, 446, 877
- Madden, S. C., Rémy-Ruyer, A., Galametz, M., et al. 2013, *PASP*, 125, 600
- Magdis, G. E., Rigopoulou, D., Helou, G., et al. 2013, *A&A*, 558, A136
- Magnelli, B., Lutz, D., Saintonge, A., et al. 2014, *A&A*, 561, A86
- Maier, C., Lilly, S. J., Ziegler, B. L., et al. 2014, *ApJ*, 792, 3
- Maiolino, R., Cox, P., Caselli, P., et al. 2005, *A&A*, 440, L51
- Maiolino, R., Nagao, T., Grazian, A., et al. 2008, *A&A*, 488, 463
- Maiolino, R., Carniani, S., Fontana, A., et al. 2015, *ArXiv e-prints*
- Mannucci, F., Cresci, G., Maiolino, R., et al. 2009, *MNRAS*, 398, 1915
- Marconi, A., Risaliti, G., Gilli, R., et al. 2004, *MNRAS*, 351, 169
- Marshall, J. A., Herter, T. L., Armus, L., et al. 2007, *ApJ*, 670, 129
- Matsuoka, K., Nagao, T., Maiolino, R., Marconi, A., & Taniguchi, Y. 2009, *A&A*, 503, 721
- . 2011, *A&A*, 532, L10
- McGreer, I. D., Jiang, L., Fan, X., et al. 2013, *ApJ*, 768, 105
- Mechtley, M., Windhorst, R. A., Ryan, R. E., et al. 2012, *ApJ*, 756, L38
- Mor, R., & Netzer, H. 2012, *MNRAS*, 420, 526
- Mor, R., & Trakhtenbrot, B. 2011, *ApJ*, 737, L36
- Morganson, E., De Rosa, G., Decarli, R., et al. 2012, *AJ*, 143, 142
- Mortlock, D. J., Patel, M., Warren, S. J., et al. 2009, *A&A*, 505, 97
- Mullaney, J. R., Alexander, D. M., Goulding, A. D., & Hickox, R. C. 2011, *MNRAS*, 414, 1082
- Muratov, A. L., Keres, D., Faucher-Giguere, C.-A., et al. 2015, *ArXiv e-prints*
- Nagao, T., Maiolino, R., De Breuck, C., et al. 2012, *A&A*, 542, L34
- Nagao, T., Maiolino, R., & Marconi, A. 2006, *A&A*, 447, 863
- Netzer, H. 2009, *MNRAS*, 399, 1907
- Netzer, H., Mor, R., Trakhtenbrot, B., Shemmer, O., & Lira, P. 2014, *ApJ*, 791, 34
- Netzer, H., Lutz, D., Schweitzer, M., et al. 2007, *ApJ*, 666, 806
- Omont, A., Willott, C. J., Beelen, A., et al. 2013, *A&A*, 552, A43
- Östlin, G., Amram, P., Bergvall, N., et al. 2001, *A&A*, 374, 800
- Östlin, G., Amram, P., Masegosa, J., Bergvall, N., & Boulesteix, J. 1999, *A&AS*, 137, 419
- Östlin, G., Hayes, M., Kunth, D., et al. 2009, *AJ*, 138, 923
- Ouchi, M., Ellis, R., Ono, Y., et al. 2013, *ApJ*, 778, 102
- Petric, A. O., Carilli, C. L., Bertoldi, F., et al. 2003, *AJ*, 126, 15

- Planck Collaboration, Adam, R., Ade, P. A. R., et al. 2015, ArXiv e-prints
- Rawle, T. D., Egami, E., Bussmann, R. S., et al. 2014, ApJ, 783, 59
- Rémy-Ruyer, A., Madden, S. C., Galliano, F., et al. 2013, A&A, 557, A95
- . 2015a, ArXiv e-prints
- . 2015b, A&A, 573, C1
- Richards, G. T., Lacy, M., Storrie-Lombardi, L. J., et al. 2006, ApJS, 166, 470
- Riechers, D. A., Walter, F., Carilli, C. L., et al. 2006, ApJ, 650, 604
- Riechers, D. A., Bradford, C. M., Clements, D. L., et al. 2013, Nature, 496, 329
- Rieke, G. H., Alonso-Herrero, A., Weiner, B. J., et al. 2009, ApJ, 692, 556
- Rodighiero, G., Daddi, E., Baronchelli, I., et al. 2011, ApJ, 739, L40
- Rosario, D. J., Santini, P., Lutz, D., et al. 2012, A&A, 545, A45
- Rujopakarn, W., Rieke, G. H., Eisenstein, D. J., & Juneau, S. 2011, ApJ, 726, 93
- Rujopakarn, W., Rieke, G. H., Weiner, B. J., et al. 2013, ApJ, 767, 73
- Runnoe, J. C., Brotherton, M. S., & Shang, Z. 2012, MNRAS, 422, 478
- Sajina, A., Yan, L., Fadda, D., Dasyra, K., & Huynh, M. 2012, ApJ, 757, 13
- Salim, S., Rich, R. M., Charlot, S., et al. 2007, ApJS, 173, 267
- Salpeter, E. E. 1955, ApJ, 121, 161
- Schneider, R., Bianchi, S., Valiante, R., Risaliti, G., & Salvadori, S. 2014, ArXiv e-prints
- Schreiber, C., Pannella, M., Elbaz, D., et al. 2015, A&A, 575, A74
- Scott, A. E., & Stewart, G. C. 2014, MNRAS, 438, 2253
- Shang, Z., Brotherton, M. S., Wills, B. J., et al. 2011, ApJS, 196, 2
- Sugiura, N. 1978, Communications in Statistics-Theory and Methods, 7, 13
- Symeonidis, M., Page, M. J., Seymour, N., et al. 2009, MNRAS, 397, 1728
- Symeonidis, M., Vaccari, M., Berta, S., et al. 2013, MNRAS, 431, 2317
- Targett, T. A., Dunlop, J. S., & McLure, R. J. 2012, MNRAS, 420, 3621
- Valiante, R., Schneider, R., Bianchi, S., & Andersen, A. C. 2009, MNRAS, 397, 1661
- Walter, F., Carilli, C., Bertoldi, F., et al. 2004, ApJ, 615, L17
- Walter, F., Riechers, D., Cox, P., et al. 2009, Nature, 457, 699
- Wang, J.-M., Yan, C.-S., Gao, H.-Q., et al. 2010a, ApJ, 719, L148
- Wang, J.-M., Ge, J.-Q., Hu, C., et al. 2011a, ApJ, 739, 3
- Wang, R., Wagg, J., Carilli, C. L., et al. 2008a, AJ, 135, 1201
- Wang, R., Carilli, C. L., Wagg, J., et al. 2008b, ApJ, 687, 848
- Wang, R., Carilli, C. L., Neri, R., et al. 2010b, ApJ, 714, 699
- Wang, R., Wagg, J., Carilli, C. L., et al. 2011b, ApJ, 739, L34
- . 2011c, AJ, 142, 101
- . 2013, ApJ, 773, 44
- Watson, D., Christensen, L., Knudsen, K. K., et al. 2015, Nature, 519, 327
- Willmer, C. N. A., Rieke, G. H., Le Floc'h, E., et al. 2009, AJ, 138, 146
- Willott, C. J., Bergeron, J., & Omont, A. 2015, ApJ, 801, 123
- Willott, C. J., Omont, A., & Bergeron, J. 2013, ApJ, 770, 13
- Willott, C. J., Albert, L., Arzoumanian, D., et al. 2010a, AJ, 140, 546
- Willott, C. J., Delorme, P., Reylé, C., et al. 2010b, AJ, 139, 906
- Wright, E. L., Eisenhardt, P. R. M., Mainzer, A. K., et al. 2010, AJ, 140, 1868
- Wu, Y., Charmandaris, V., Hao, L., et al. 2006, ApJ, 639, 157
- Wu, Y., Charmandaris, V., Hunt, L. K., et al. 2007, ApJ, 662, 952
- Xu, L., Rieke, G. H., Egami, E., et al. 2015a, ApJ, 808, 159
- . 2015b, ApJS, 219, 18
- Zafar, T., Möller, P., Ledoux, C., et al. 2011, A&A, 532, A51

APPENDIX

A. TEMPLATES FOR DWARF GALAXIES

A.1. Sample and Infrared Data

The sample used to compute the SEDs of low-metallicity galaxies is from the Dwarf Galaxy Survey (DGS; Madden et al. 2013). This sample covers the full metallicity range observable in the local Universe with $12+\log(\text{O}/\text{H})$ ranging from 7.14 to 8.43, and spans four orders of magnitude in star formation rates.

The far-IR data adopted here is mainly from Rémy-Ruyer et al. (2013)⁸. A total of 48 dwarf galaxies were observed with PACS and SPIRE on board of the *Herschel Space Observatory* at 70, 100, 160, 250, 350, and 500 μm . For I Zw 18, we update with the *Herschel* data from Fisher et al. (2014). We also collect the near-IR to mid-IR photometry data for the whole sample from the *Wide-field Infrared Survey Explorer* (WISE; Wright et al. 2010) at 3.4, 4.6, 12 and 22 μm . 47 of these galaxies were found to have low-resolution mid-IR spectroscopic observations from the *Spitzer* archive. We collect the staring-mode *Spitzer*/IRS spectra from the Cornell Atlas of *Spitzer*/IRS Sources (CASSIS; Lebouteiller et al. 2011)⁹ and adopt the post-BCD products from the *Spitzer* Heritage Archive (SHA) for mapping-mode observations, which were reduced in the SSC Pipeline Version S18.18. The latter spectral

⁸ Rémy-Ruyer et al. (2015b) corrected the PACS photometry for three galaxies, HS 0822+3542, HS 1442+4250 and Tol 0618. However, none of our arguments made in the appendix would be changed.

⁹ The Cornell Atlas of *Spitzer*/IRS Sources (CASSIS) is a product of the Infrared Science Center at Cornell University, supported by NASA and JPL.

maps are combined into a single spectrum to represent the mid-IR emission continuum of the galaxy. However, since the surface brightnesses of dwarf galaxies are typically low, only a few *Spitzer* spectra have high enough signal-to-noise ratio (S/N) continuum to be useful for our derivation of the full IR SEDs. Finally, we focus on 19 DGS galaxies to study their IR SEDs.

A.2. SED Modeling and Template Construction¹⁰

In Rémy-Ruyer et al. (2013), a simple modified blackbody is fit to the far-IR photometry of the DGS sample to derive dust properties like temperature, mass, and emissivity index. After introducing the WISE mid-IR data at 12 and 22 μm , the far-IR SED peak shifts towards a shorter wavelength for the majority of sources, leading to a higher dust temperature. One single (modified) blackbody is not enough to represent the full IR SED, since galaxies always have a range of dust temperatures (e.g., Dunne & Eales 2001; Willmer et al. 2009; Galametz et al. 2012; Kirkpatrick et al. 2012).

Here we utilize the Casey (2012) procedure (hereafter CMC fits) to address the mid-IR excess. Casey (2012) developed a fitting routine to fit the IR data points with a modified blackbody plus a power-law component. The mid-IR component is described as an analytical function

$$S(\lambda)_{\text{MIR}} = N_{\text{MIR}} \lambda^{\alpha} e^{-(\lambda/\lambda_c)^2}, \quad (\text{A1})$$

where α is the mid-IR power-law slope, and λ_c the power-law turnover wavelength. The normalizing factor $N_{\text{mid-IR}}$ and turnover wavelength λ_c are bounded with other parameters. We relax the bounding condition of

¹⁰ After the submission of this paper, a comprehensive study of the physical basis of the infrared SEDs of the DGS sample of galaxies was published by Rémy-Ruyer et al. (2015a). Their conclusions about the general shape of the SEDs are similar to ours.

λ_c to fit the diverse SEDs of the DGS sample, leaving other configurations unchanged (see Casey 2012). Since the light from old stellar populations may contribute to the SED (mainly at short wavelengths), we assume the emission in the WISE W1 band is completely stellar and scale a Rayleigh-Jeans tail to estimate the stellar contribution to other bands. The final SED fit is done for $\lambda > 8\mu\text{m}$ data points after subtracting the possible old population stellar contribution from the observed fluxes.

In Table 7, we list the basic information and fit parameter values. In Figure 9, we show the SED continuum fits for the 19 DGS galaxies. We also present the results of single modified blackbody fits (only on *Herschel* data) for comparison.

Figure 10 shows the full infrared SEDs (after adding the *Spitzer* spectra) for the 19 DGS galaxies. The mid-IR continua derived from the photometry fitting and those directly obtained from the mid-IR spectra are consistent. The mid-infrared regions of these low-metallicity objects present substantial forbidden line emissions and weak or no PAH emission (e.g., Wu et al. 2006, 2007), which contribute little to the continuum. For the final model SEDs of the 19 DGS galaxies, we discard the mid-IR portion of the fit SED continua based on WISE and *Herschel* photometry, and replace it with scaled *Spitzer* spectra.

A.3. Features of low-metallicity galaxy templates

Figure 11 compares the 19 low-metallicity templates with the normal SF galaxy templates in Rieke et al. (2009). The SEDs of these dwarf galaxies show a lot of variation. Compared with the solar-metallicity galaxies, the low-metallicity infrared SEDs derived in this work tend to have the following features:

- Higher far-IR dust temperature. For the low-metallicity galaxies, the typical dust temperature is $T_{\text{dust}} = 34 \pm 7.7$. Our value is similar to the result by Rémy-Ruyer et al. (2013) ($T_{\text{dust}} \sim 32\text{K}$). Compared with the *Herschel* KINGFISH sample ($T_{\text{dust}} \sim 23\text{K}$, Rémy-Ruyer et al. 2013), which contains more metal-rich environments, the dust in these low-metallicity systems is generally warmer;
- Steeply rising mid-IR continua. For low-metallicity galaxies in this work, the mid-IR continua slope $\alpha = 3.8 \pm 0.8$, which is much larger than typical values in normal galaxies ($\alpha = 2.0 \pm 0.5$ in Casey 2012; $1.7\text{--}2.2$ in Blain et al. 2003);
- Weaker aromatic features. The contribution of aromatic features to the infrared SED of low-metallicity galaxies is substantially lower than normal galaxies. The weaker aromatic features with decreasing metallicity have been reported by many authors (e.g., Engelbracht et al. 2005, 2008; Madden et al. 2006).

All of these features can be explained by a rich population of small (and/or hot) grains in the low-metallicity environments (e.g., Madden et al. 2006). In addition, some authors also report mm excess emission in these dwarf systems (e.g., Galliano et al. 2003, 2005; Galametz et al. 2009). Since the origin of this excess is not clear and its contribution to the infrared luminosity is tiny, we do not consider it in this work.

B. STAR FORMATION IN DWARF GALAXIES

B.1. Star Formation Determination

The star formation rate can be estimated by the 8-1000 μm infrared emission, following the Kennicutt (1998) star formation law,

$$\text{SFR}(\text{IR}, M_{\odot}/\text{yr}) = 4.5 \times 10^{-44} L(\text{IR}, \text{erg/s}). \quad (\text{B1})$$

This relation is widely used for high- z galaxies though it was originally established for star-bursting galaxies. However, it is not clear if and how it is valid for low-metallicity dwarf galaxies.

In general, the star formation in a galaxy can be both dust-obscured and dust-unobscured. For unobscured star formation, tracers that probe direct stellar light (e.g., the GALEX FUV at $0.153\mu\text{m}$) or ionized gas tracers (e.g., $H\alpha$, $\text{Pa}\alpha$) are used. For dwarf galaxies, Lee et al. (2009) find FUV has a better performance than $H\alpha$ to trace the star formation, since the latter tends to underpredict the total SFR relative to the FUV for low luminosity systems. Therefore we use the FUV star formation law derived in Salim et al. (2007), a study that includes dwarf galaxies, to calculate the dust-unobscured star formation rate:

$$\text{SFR}(\text{FUV}, M_{\odot}/\text{yr}) = 1.08 \times 10^{-28} L_{\nu}(\text{FUV}, \text{erg/s/hz}). \quad (\text{B2})$$

The dust-obscured star formation can be determined from the dust-processed light at wavelengths where dust emission dominates (e.g., the $24\mu\text{m}$ emission, the total infrared emission). We use MIPS $24\mu\text{m}$ star formation law in Rieke et al. (2009):

$$\text{SFR}(24\mu\text{m}, M_{\odot}/\text{yr}) = 2.02 \times 10^{-43} L(24\mu\text{m}, \text{erg/s}). \quad (\text{B3})$$

The final star formation rates of these dwarf galaxies are assumed to be a sum of these two components, which will be compared with that derived from the total infrared luminosity (Equation B1).

We collect GALEX FUV and MIPS $24\mu\text{m}$ data to derive the star formation. All of the 19 dwarf galaxies above have MIPS $24\mu\text{m}$ observations, and 14/19 have GALEX FUV observations. We retrieve their photometry from the catalog of Spitzer Enhanced Imaging Products¹¹ and the GALEX official online catalog¹². IC10, NGC 4214, UM 311, VII Zw 403 are either too extended or have a close companion in their MIPS $24\mu\text{m}$ images, thus they were removed from the comparison. GALEX FUV photometry can be found for all sources with MIPS observations.

In Figure 12, we compare the star formation rates derived from the 8-1000 μm infrared emission and those derived from the combined GALEX FUV and MIPS $24\mu\text{m}$ emission. Within a three order-of-magnitude dynamical range, the star formation rates from these two approaches are generally consistent, without any obvious offset due to metallicity effect. Thus, we conclude the behavior of Kennicutt (1998) L_{TIR} star formation law is similar to other star formation indicators for the population of dwarf galaxies, at least for those studied in this work, and not very sensitive to metallicity.

¹¹ <http://irsa.ipac.caltech.edu/data/SPITZER/Enhanced/SEIP/overview>.

¹² <http://galex.stsci.edu/GalexView/>

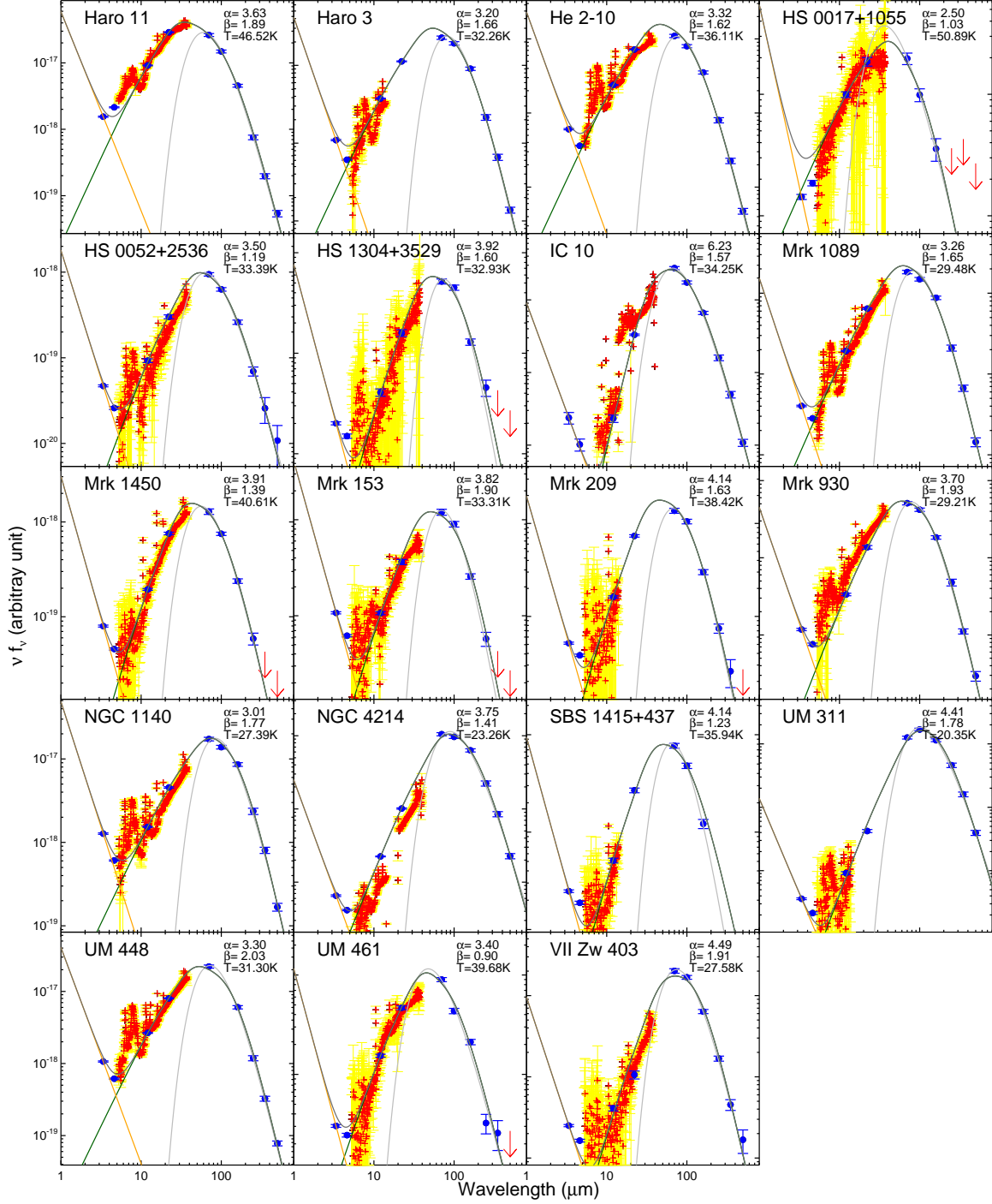


FIG. 9.— IR SEDs of the 19 DGS galaxies. Blue circles are for detections and red down arrows are for upper limits. The available *Spitzer*/IRS spectrum for each source (red crosses for the flux, yellow shadows for the flux error) is also plotted. We first subtract the stellar light in the SED by assuming a Rayleigh-Jeans tail scaled by the WISE W1 band data point, then fit the data points at 8-1000 μ m with the modified blackbody + mid-IR power-law model (namely, CMC fits, green lines). The final model SED is shown as dark grey lines. The T , α , and β parameters derived from the CMC fits are indicated on the right up corner of each panel. In a similar fashion as Rémy-Ruyer et al. (2013), a single modified blackbody is also fit to the *Herschel* data points for comparison (light grey line).

TABLE 7
LOW-METALLICITY GALAXIES USED TO DERIVE THE TEMPLATES

Source (1)	12+log(O/H) (2)	T _{dust} (K) (3)	β (4)	α (5)	Mid-IR Spectrum? (6)
Haro 11	8.36±0.01	46.5±1.0	1.89	3.63	good
Haro 3	8.28±0.01	32.3±0.9	1.66	3.20	limited
He 2-10	8.43±0.01	36.1±0.7	1.62	3.32	good
HS 0017+1055	7.63±0.10	50.9±8.2	1.03	2.50	good
HS 0052+2536	8.04±0.10	33.4±2.1	1.19	3.50	good
HS 1304+3529	7.93±0.10	33.9±2.6	1.60	3.92	good
IC 10	8.17±0.03	34.3±0.8	1.57	6.23	poor
Mrk 1089	8.10±0.08	29.5±1.0	1.65	3.26	good
Mrk 1450	7.84±0.01	40.6±1.5	1.39	3.91	good
Mrk 153	7.86±0.04	33.3±2.3	1.90	3.82	good
Mrk 209	7.74±0.01	38.4±1.2	1.63	4.14	limited
Mrk 930	8.03±0.01	29.2±1.7	1.93	3.70	good
NGC 1140	8.38±0.01	27.4±1.0	1.77	3.01	good
NGC 4214	8.26±0.01	23.3±0.7	1.41	3.75	limited
SBS 1415+437	7.55±0.01	38.9±3.2	1.23	4.14	limited
UM 311	8.36±0.01	20.4±0.7	1.78	4.41	limited
UM 448	8.32±0.01	31.3±1.0	2.03	3.30	good
UM 461	7.73±0.01	40.0±2.0	0.90	3.40	good
VII Zw 403	7.66±0.01	27.6±1.8	1.91	4.49	good

NOTE. — Col. (1): The galaxy name; Col. (2) The metallicity 12+log(O/H); Col. (3): The dust temperature derived from the CMC fit (see text); Col. (4): The far-IR emission index; Col. (5): The mid-IR power-law index; Col. (6): The existence of the mid-IR *Spitzer* spectrum: *good* – the galaxy has full range 5–35 μ m mid-IR spectrum; *limited* – the galaxy has mid-IR spectrum with limited coverage; *poor* – IC 10 is quite extended, as judged from its MIPS 24 μ m image, making the *Spitzer* spectrum a poor reflection of the overall mid-IR continuum.

TABLE 8
THE STAR FORMATION RATES OF THE DWARF GALAXIES

Source (1)	12+(O/H) (2)	L_{IR} ($10^{11} L_{\odot}$) (3)	SFR _{IR} (M_{\odot}/yr) (4)	SFR _{FUV} (M_{\odot}/yr) (5)	SFR _{24μm} (M_{\odot}/yr) (6)	SFR _{FUV+24μm} (M_{\odot}/yr) (7)
Haro 11	8.36±0.01	1.77	30.60	3.37	56.06	59.43
Haro 3	8.28±0.01	0.057	0.99	0.22	0.82	1.04
He 2-10	8.43±0.01	0.061	1.05	–	1.13	–
HS 0017+1055	7.63±0.10	0.0095	0.16	–	0.26	–
HS 0052+2536	8.04±0.10	0.18	3.07	1.57	1.88	3.45
HS 1304+3529	7.93±0.01	0.017	0.30	–	0.18	–
IC 10	8.17±0.03	0.000055	0.00095	–	–	–
Mrk 1089	8.10±0.08	0.35	6.10	2.40	3.49	5.89
Mrk 1450	7.84±0.01	0.0030	0.053	–	0.064	–
Mrk 153	7.86±0.04	0.0098	0.17	0.67	0.12	0.79
Mrk 209	7.74±0.01	0.00029	0.0051	0.012	0.0046	0.017
Mrk 930	8.03±0.01	0.16	2.78	1.13	2.70	3.83
NGC 1140	8.38±0.01	0.036	0.62	0.49	0.32	0.81
NGC 4214	8.26±0.01	0.0040	0.070	0.076	–	–
SBS 1415+437	7.25±0.01	0.00070	0.012	0.033	0.0094	0.042
UM 311	8.36±0.01	0.037	0.65	0.21	–	–
UM 448	8.32±0.01	0.88	15.15	2.19	11.76	13.95
UM 461	7.73±0.01	0.00091	0.016	0.0010	0.017	0.028
VII Zw 403	7.66±0.01	0.00016	0.0028	0.0065	–	–

NOTE. — Objects with ‘–’ in Column (5), (6) do not have corresponding observations or are not point-sources to be included in the catalogs (see text).

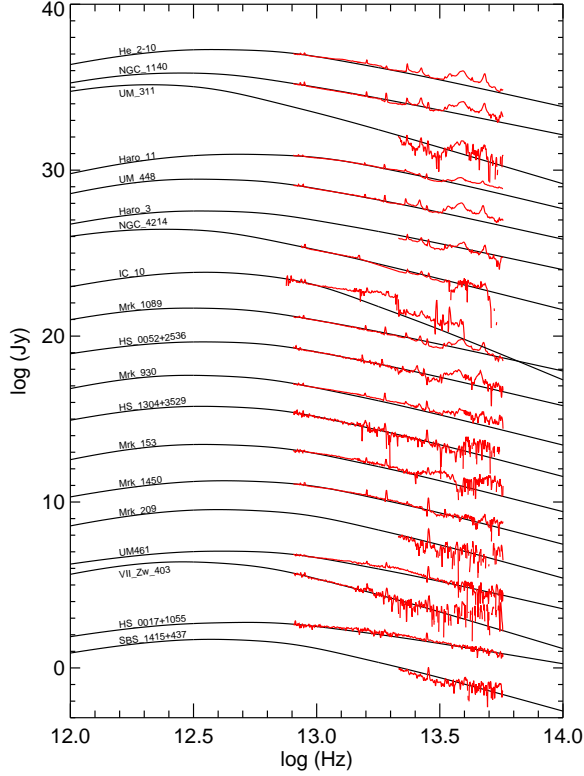


FIG. 10.— Full IR SEDs of the 19 DGS galaxies that have *Spitzer*/IRS low-resolution spectra with high enough S/N, sequenced by their metallicity with the lowest at the bottom. The *Spitzer* spectra are scaled to match the continuum SEDs.

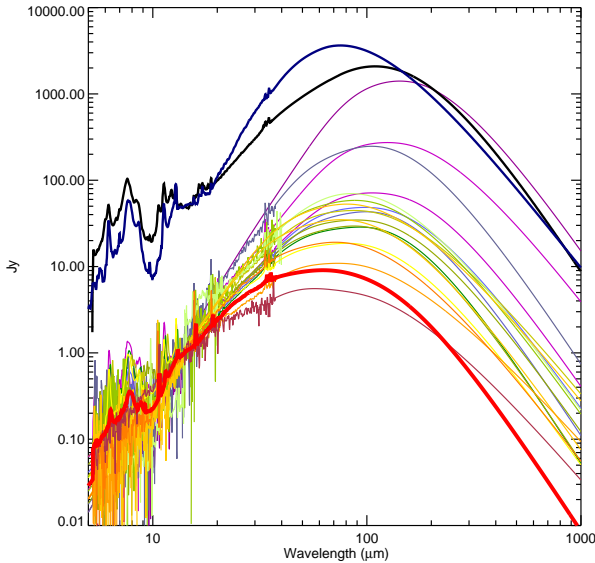


FIG. 11.— Family of full IR SEDs of the 19 DGS galaxies, normalized at rest-frame $14\mu\text{m}$ (bottom group). We use thick red line to highlight the SED of Haro 11. For comparison, we present two normal SF SED templates in Rieke et al. (2009): $\log(L/L_\odot) = 12$ (thick blue line), 11 (thick black line).

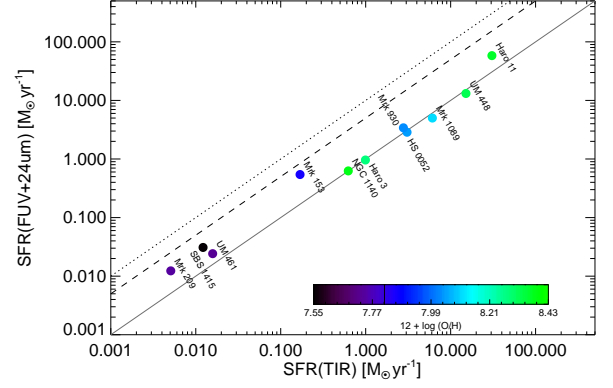


FIG. 12.— Comparison of star formation rates (SFRs) from the total infrared luminosity (8-1000 μm) and those from GALEX FUV + MIPS 24 μm . The colors code the metallicity $12+\log(\text{O}/\text{H})$. As a guide to the eye, we also show the one-to-one (gray solid line), one-to-five (gray dashed line), and one-to-ten (gray dotted line) lines.

B.2. Star Formation Law of Haro 11

As discussed in Section 2, Haro 11 was selected as the candidate galaxy template for high- z galaxies. With ample observations presented in the literature, its star formation rate can be estimated using various star-formation indicators, including the 8-1000 μm infrared luminosity, MIPS 24 μm emission, $H\alpha$ emission-line luminosity, and FUSE/GALEX FUV luminosity. Following the calibrations listed above, we estimate its star formation rates and summarize these results in Table 9.

The SFR determined from the 24 μm emission is ~ 1.8 times higher than that from either L_{IR} or $L(H\alpha)$. This discrepancy is a direct consequence of its hot SED (Engelbracht et al. 2008) and the resulting large fraction of its L_{IR} emitted at 24 μm (see Figure 13)¹³. Given the close agreement in the SFRs from $H\alpha$ and L_{IR} , we conclude that Haro 11 falls above the trend line in Figure 12 because FUV+24 μm overestimates the SFR and L_{IR} gives a valid estimate. Moreover, since Haro 11 presents very young stellar populations (Adamo et al. 2010), the contamination of emission from old stars to the far infrared emission is negligible, which makes the L_{IR} , following the Kennicutt (1998) SF law, a robust tracer of the obscured star formation.

We use the FUV luminosity based on GALEX observation and assume the star formation law in Salim et al. (2007) to estimate the unobscured star formation. The final adopted star formation rate of Haro 11, which is $34.0 M_\odot/\text{yr}$, is based on a combination of GALEX FUV emission and the 8-1000 μm infrared emission. We can finally relate the infrared luminosity and FUV luminosity of Haro 11 to its total star formation rate, which includes both the obscured and the unobscured, as

$$\text{SFR}_{\text{Haro 11}}(M_\odot/\text{yr}) = 5.00 \times 10^{-44} L(\text{IR}, \text{erg/s}) \quad (\text{B4})$$

$$= 1.92 \times 10^{-10} L(\text{IR}, L_\odot) \quad (\text{B5})$$

This is the star formation law used for the Haro 11 tem-

¹³ Another galaxy with $\text{SFR}(24\mu\text{m})/\text{SFR}(\text{FIR}) > 1.25$ in our low-metallicity galaxy sample is Mrk 153, which hosts an AGN that boosts the mid-IR emission.

TABLE 9
STAR FORMATION RATE OF HARO 11

Method	Luminosity (L_{\odot}) ^a	SFR (M_{\odot}/yr)	SFR Law	Reference
L_{IR}	1.8×10^{11}	30.6	Kennicutt (1998)	this work
MIPS 24 μm	6.7×10^{10}	56.1	Rieke et al. (2009)	this work
$\text{H}\alpha$ (Fabry-Perot) ^b	1.3×10^9	39.1	Kennicutt et al. (1994)	Östlin et al. (1999)
$\text{H}\alpha$ (HST image) ^b	8.7×10^8	25.7	Kennicutt et al. (1994)	Östlin et al. (2009)
GALEX FUV (0.153 μm) ^c	1.6×10^{10}	3.4	Salim et al. (2007)	this work
FUSE FUV (0.115 μm) ^c	2.2×10^{10}	4.5	Kennicutt (1998)	Grimes et al. (2007)

NOTE. — ^a All luminosities are scaled to the distance 92.1 Mpc (Bergvall et al. 2006). ^b We corrected the $\text{H}\alpha$ extinction based on the observed Balmer decrement $\text{H}\alpha/\text{H}\beta = 4.08$ (Bergvall & Östlin 2002) with the assumption of an intrinsic ratio 2.85 and a Calzetti (2001) extinction law. The attenuation at V-band is estimated to be $A_V = 0.95$, suggesting the intrinsic $\text{H}\alpha$ flux would be a factor of 1.34 larger than the observed. ^c For the UV band, since we do not make extinction corrections, the SFR(FUV) listed here are only for unobscured star formation.

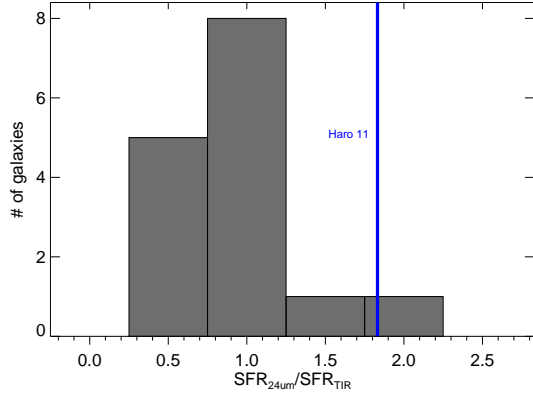


FIG. 13.— Histogram of the ratio between the 24 μm -based SFR and L_{IR} -based SFR of dwarf galaxies. Haro 11 has a $\text{SFR}(24\mu\text{m})/\text{SFR}(\text{TIR})$ 1.82 as denoted in the blue line.

plate in the main part of this paper.